AFRL-RY-WP-TR-2014-0233

NEW CONCEPTS IN ELECTROMAGNETIC MATERIALS AND ANTENNAS

Jeffrey Allen, Naftali Herscovici, Brad Kramer, and Bae-Ian Wu

Antennas & Electromagnetics Technology Branch
Multispectral Sensing & Detection Division

JANUARY 2015
Final Report

STINFO COPY

AIR FORCE RESEARCH LABORATORY
SENSORS DIRECTORATE
WRIGHT-PATTERSON AIR FORCE BASE, OH 45433-7320
AIR FORCE MATERIEL COMMAND
UNITED STATES AIR FORCE

NOTICE AND SIGNATURE PAGE

*//Signature//

BRADLEY A. KRAMER, Program Manager
Antenna & Electromagnetic Technology Branch
Multispectral Sensing & Detection Division

//Signature//

TONY C. KIM, Branch Chief
Antenna & Electromagnetic Technology Branch
Multispectral Sensing & Detection Division

*//Signature//

TRACY W. JOHNSTON, Division Chief
Multispectral Sensing & Detection Division
Sensors Directorate

REPORT DOCUMENTATION PAGE				Form Approved OMB No. 0704-0188

The public reporting burden for this collection of information is estimated to average 1 hour per response, including the time for reviewing instructions, searching existing data sources, searching existing data sources, gathering and maintaining the data needed, and completing and reviewing the collection of information. Send comments regarding this burden estimate or any other aspect of this collection of information, including suggestions for reducing this burden, to Department of Defense, Washington Headquarters Services, Directorate for Information Operations and Reports (0704-0188), 1215 Jefferson Davis Highway, Suite 1204, Arlington, VA 22202-4302. Respondents should be aware that notwithstanding any other provision of law, no person shall be subject to any penalty for failing to comply with a collection of information if it does not display a currently valid OMB control number. **PLEASE DO NOT RETURN YOUR FORM TO THE ABOVE ADDRESS**.

1. REPORT DATE (DD-MM-YY) January 2015	2. REPORT TYPE Final	3. DATES COVERED (From - To) 1 October 2011 – 30 June 2014

4. TITLE AND SUBTITLE NEW CONCEPTS IN ELECTROMAGNETIC MATERIALS AND ANTENNAS	5a. CONTRACT NUMBER In-house
	5b. GRANT NUMBER
	5c. PROGRAM ELEMENT NUMBER 61102F
6. AUTHOR(S) Jeffrey Allen, Naftali Herscovici, Brad Kramer, and Bae-Ian Wu	5d. PROJECT NUMBER 3001
	5e. TASK NUMBER 12RY06COR
	5f. WORK UNIT NUMBER Y0PC

7. PERFORMING ORGANIZATION NAME(S) AND ADDRESS(ES) Antennas & Electromagnetics Technology Branch (AFRL/RYMH) Multispectral Sensing & Detection Division Air Force Research Laboratory, Sensors Directorate Wright-Patterson Air Force Base, OH 45433-7320 Air Force Materiel Command, United States Air Force	8. PERFORMING ORGANIZATION REPORT NUMBER AFRL-RY-WP-TR-2014-0233

9. SPONSORING/MONITORING AGENCY NAME(S) AND ADDRESS(ES) Air Force Research Laboratory Sensors Directorate Wright-Patterson Air Force Base, OH 45433-7320 Air Force Materiel Command United States Air Force	10. SPONSORING/MONITORING AGENCY ACRONYM(S) AFRL/RYMH
	11. SPONSORING/MONITORING AGENCY REPORT NUMBER(S) AFRL-RY-WP-TR-2014-0233

12. DISTRIBUTION/AVAILABILITY STATEMENT
Approved for public release; distribution unlimited

13. SUPPLEMENTARY NOTES
PAO Case Number 88ABW-2014-5989, Clearance Date 18 December 2014. Report contains color.

14. ABSTRACT
The overall objective of this research is to develop antenna and sensor systems that will meet the Air Force's ever-increasing demand for reduced cost, size, weight, and power (CSWAP) while maintaining or increasing system functionality. This basic research effort consists of several sub-tasks that use analytical and numerical methods to examine the interaction of metamaterials and antennas, topics in transformation optics, and performance limitations of antennas on artificial magnetic grounds and unmanned aircraft systems (UAS). This interim report summarizes the first 20 months of a three year effort.

15. SUBJECT TERMS
metamaterials, transformation optics, artificial magnetic grounds, antenna array, electrically small antennas.

16. SECURITY CLASSIFICATION OF:			17. LIMITATION OF ABSTRACT: SAR	18. NUMBER OF PAGES 80	19a. NAME OF RESPONSIBLE PERSON (Monitor) Bradley A. Kramer
a. REPORT Unclassified	b. ABSTRACT Unclassified	c. THIS PAGE Unclassified			19b. TELEPHONE NUMBER (Include Area Code) N/A

Standard Form 298 (Rev. 8-98)
Prescribed by ANSI Std. Z39-18

Table of Contents

List of Figures

Figure   **Page**

iv

1   EXECUTIVE SUMMARY

The overall objective of this three year research project is to develop antenna and sensor systems that will meet the Air Force's ever-increasing demand for reduced cost, size, weight, and power (CSWAP) while maintaining or increasing system functionality. This basic research effort consists of several sub-tasks that use analytical and numerical methods to examine the interaction of metamaterials and antennas, topics in transformation optics, and performance limitations of antennas on artificial magnetic grounds and unmanned aircraft systems (UAS). Specifically, this in-house research and development program consists of four sub-tasks which are: 1) Metamaterial Inspired Superstrates for Smart Antenna Systems (Dr. Jeffery Allen). 2) Bandwidth Limitations of Antennas on Artificial Magnetic Grounds (Dr. Herscovici). 3) Topics in Transformation Optics and Metamaterials (Dr. Bae-Ian Wu). 4) Fundamental Performance Limitations of Antennas Mounted on Electrically Small UAS (Dr. Kramer). The objective(s) for each sub-task is briefly stated below.

1. Subtask 1: Metamaterial Inspired Superstrates for Smart Antenna Systems
   - Create simplified methods that combine material and physical modeling approaches to understand how the behavior of phased array antenna systems can be modified using metamaterial superstrates.
2. Subtask 2: Bandwidth Limitations of Antennas on Artificial Magnetic Grounds
   - The objective is to determine and compare bandwidth limitations of antennas on artificial magnetic grounds (AMG) and traditional perfectly conducting (PEC) ground planes as a function of the separation between antenna and the AMG/PEC plane. The goal is to examine the trade-off between bandwidth and separation for the two types of ground planes that are common to low-profile antennas.
3. Subtask 3: Topics in Transformation Optics and Metamaterials
   - In the first year of research, the objectives from the proposed graphene study are to yield a better understanding of electromagnetics in graphene-based structures and provide new theoretical tools regarding the guidance properties of graphene-based transmission line for metamaterial devices and sensors in the mm-wave and optical frequencies.
   - For the transformation optics/metamaterial research, the objectives would be to establish a working code based on analytic technique for the study of the antenna problem. The configuration for such hybrid analytic studies will be of canonical shapes, including planar, cylindrical, and spherical with or without the presence of ground plane. Conformal antenna based on transformation optics would be the next step. At the same time, the feasibility of using spectral transformation and surface current based media inversion is expected to be completed by the first year mark.
4. Subtask 4: Fundamental Performance Limitations of Antennas Mounted on Electrically Small Unmanned Aircraft Systems (UAS)
   - The goal of this effort is to establish performance limits for antennas mounted on structures (e.g. UAS, Micro-UAS, etc.) with sub-wavelength dimensions.

The remainder of this report discusses the objectives in more detail and summarizes the results of the first 20 months of this three year project.

2 Subtask 1: Metamaterial Inspired Superstrates for Smart Antenna Systems

In compact phased arrays, only a small number of antenna elements are available. This directly determines and limits the number of degrees of freedom that are available for adaptive beam/null-forming. It limits the number of nulls/beams that the system can steer, where these null/beams can be placed and their quality as well as the gain of the system [1]. Therefore, for a given processing algorithm, system performance can be improved either by increasing the number of antennas available, increasing how efficiently the aperture is being used, or preferentially moving available performance (e.g. ability to suppress jammers) to critical areas of scan space thus improving performance in those regions. The use of quasi-optical elements to enhance the performance of phased array anti-jam and beam steering systems has been and continues to be of great practical interest. Recent developments in engineered materials suggest even greater design possibilities for overcoming system limitations than were previously available with standard dielectric materials. Metamaterial-based devices provide additional degrees of design freedom (e.g. inhomogeneity, anisotropy, tenability, etc.) in defining the precisely spatially distributed material parameters and the ability to adjust and optimize them so as to balance the various tradeoffs in the system.

2.1 Objectives

Our objective is to use numerical approximation methods to reduce the complexity of metamaterial superstrate designs. The research will focus on developing a simplified methodology to solve the inverse problem which uses the system behavior described by the far-field radiation characteristics to calculate the material parameters that result in the required performance. We will develop this method in the context of metamaterial superstrates that give the desired system performance in antennas, phased array antenna and scattering. This investigation also aims to show how metamaterial superstrates can be designed to improve far-field characteristics, scattering problems and overall system performance of antenna systems.

2.2 Technical Summary

2.2.1 First Year Summary

During 2012 this subtask consisted of setting up, configuring and coding the software problem in Matlab and computational electromagnetic solvers (Comsol [2] and HFSS [3]). In addition, we developed analytical and full-wave electromagnetic simulation models for the scattering problem to show the efficacy of using basis functions as a method to optimize material properties that result in a desired effect such as a predefined far-field pattern or reduction in scattering cross-section. Conducted detailed literature search to help devise novel models to accurately determine and modify material properties of given electromagnetic structure. We also setup up requisite hardware (high performance computational computer for multi-threading) in conjunction with configuration of computational software to maximize performance and speed of aforementioned simulations.

Our initial problem has concentrated on controlling the scattering of cylinders. Using basis functions to represent the spatial distribution of material properties, we started exploring the inverse problem of minimizing scattering or shaping the far-field scattering profile to a pre-defined profile. This task began in fiscal year (FY) 2011, and is scheduled to be completed in FY13. Next year we plan to continue working on the scattering problem and also extend the model to the radiation problem. Specifically, we will modify the current setup to include calculation of metrics (e.g. total scattering cross section) that measure the performance of the simulations. We will then extend the simulations to three dimensions.

2.2.2   Second Year Summary

During 2013 this subtask consisted of two major objectives: demonstration of a passive optimized component (lens) and inclusion of active source into the passive transformed space for a cohesive combined transformation. We use the source transformations approach to manipulate antenna arrays such that the physical location/shape is dictated by the system (e.g. wing/fuselage) and the electromagnetic performance is defined by the application. Numerical simulations how an array with sources arranged in a circular manner can be surrounded by a transformation optics medium so that it can be made to receive and radiate as if it were a linear array of uniformly spaced elements and vice versa. We have finished setting up, configuring and coding the software problem in Matlab and computational electromagnetic solvers (Comsol) for full-wave electromagnetic simulation models where the shape of individual sources was changed using Source Transformation Optics (STO). This first set of simulations provided solutions to the ideal case and valuable information into the upper bounds defined by the physics of the problem. This information will be used in optimization routines to develop appropriate approximate Transformation Optics (TO) media with practical parameters that can be fabricated and measured using standard testing procedures. Several research methods exist to design novel engineered materials such as metamaterials to control the radiation patterns of antennas/arrays and also the scattering of objects illuminated by radiation to give some desired output. These include the following:
- Develop theoretical models to advance understanding of how device and material parameters as well as geometry of structures affects device performance
- Design simulation studies to analyze the effect of constituent material design parameters on field patterns, aperture efficiency, resonances, scattering cross-section and impedance of a device
- Develop appropriate figures-of-merit to analyze the efficacy of the design approach as well as the computational efficiency of the modeling method
The challenges are that (i) the problem has no closed form solution and therefore optimization using full-wave electromagnetic simulations required; (ii)approach can be computationally intensive and time consuming; and (ii) application of simple optimization using in-built routines in the FEM software package are not efficient and also do not produce the required results. The solution is to design a method that gives desired behavior and also produces practical device parameters in a computationally efficient model. AF mission depends on increasingly more sophisticated devices with unique properties not available in natural materials that can be accessed using application-specific engineered materials and metamaterials. This work has direct implications to the application of metamaterials to reduce the vulnerability of systems to threats such as jamming and anti-satellite weapons used in Precision Navigation and

4

Timing in GPS-Denied Environments. An example of spatial distribution of material properties to control desired device characteristics such as far-fields and scattering parameters is shown below.
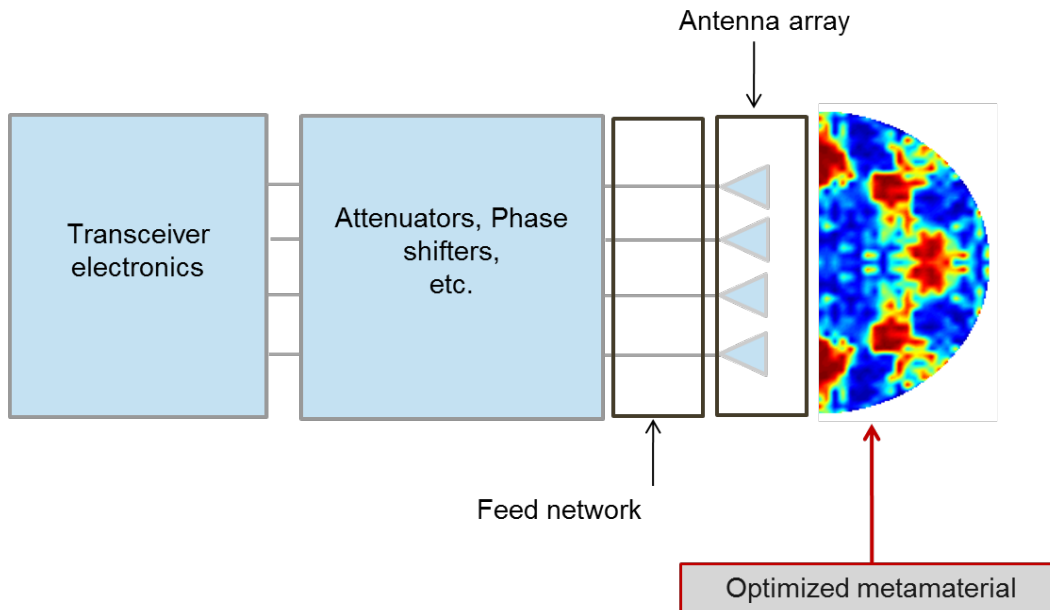
Figure 1: Example Setup of Superstrate is a Transmission System

Superstrates can be designed for radiation pattern control and to steer a beam moving the position of the source using deterministic material parameter distribution similar to a Luneburg lens. They can also be used for scattering parameters control. A cylinder illuminated by a plane wave can be coated with an engineered material to reduce its total scattering cross section. Transformation optics (TO) defines the forward problem. This methodology for designing media to control waves using accurately designed permittivity and permeability. Coordinate transforms can be used in form-invariant Maxwell equations. Demonstrated examples of TO include Cloaks, beam shifters, and concentrators. One salient example of TO is the electromagnetic cloak. An object is surrounded by a metamaterial that guides incident waves to original trajectory. To the external observer, wavefront appears undisturbed.
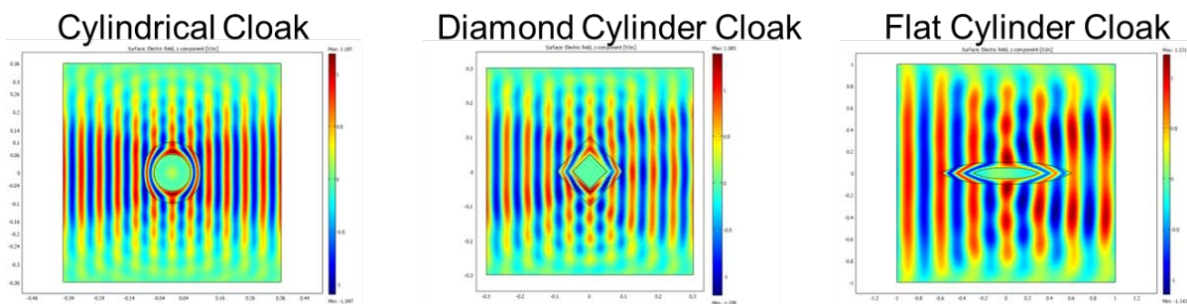
Ref: .Allen, J., N. Kundtz, D. Roberts, S. A. Cummer, and D. R. Smith, Source transformations using superellipse equations, Applied Physics Letters, v. 94, 194101, 2009.

Figure 2: Demonstrated Examples of Transformation Optics Based Cloaks

Approved for public release; distribution is unlimited.

All the approaches discussed solve the forward problem. The inverse problem is more interesting from a practical standpoint but also more difficult. The complex space with many parameters makes the problem intractable. This problem gets worse in 3D and can be very computationally intensive and can result in unrealistic material parameters. Optimization provides a route to simple solutions to these problems. Some results using optimization are discussed below.One way to solve the inverse problem is to divide the solution space (material) into differential volumes and use an optimization routine to obtain a desired result such as a reducing the scattering cross section of an object. This can create very large solution spaces that are time consuming, computationally intensive and very difficult for the most advanced optimization routines which can get stuck in a local minima. One solution is to reduce the number of parameters yet keep precision of the solution and output behavior required using smart optimization. The goals of our approach are to (i) Solve the inverse problem to get desired behavior in two different scenarios as follows. Specifically attempt to change the scattering cross-section, and reduce scattering cross-section. Secondly, change far-field pattern of a given source to mimic that of another predetermined source. We achieved this by reducing the parameters in the solution space and constraining solutions to practical material parameters. We used basis functions to represent the solution space, i.e. spatial material properties. We started with Zernike polynomials (basis functions) as shown below:

2D Zernike functions :

$$\begin{Bmatrix} Z_n^m(r,\theta) \\ Z_n^{-m}(r,\theta) \end{Bmatrix} = R_n^m(r) \begin{Bmatrix} \sin(m\theta) \\ \cos(m\theta) \end{Bmatrix}$$

where

$$R_n^m(r) = \sum_{k=0}^{\frac{(n-m)}{2}} \frac{(-1)^k (n-k)!}{k!\left(\frac{n+m}{2}-k\right)!\left(\frac{n-m}{2}-k\right)!} \quad n = 0,1,2,\dots \ (n\text{-}m) \ \text{even}$$

R : radial polynomial, n = 0,1,2,… :index represents degree of function and, m = -n to +n, (n-m) even, order. Functions are orthogonal over unit circle,

$$\iint_{\text{Over the unit circle}} Z_n^m(r,\theta) Z_{n'}^{m'}(r,\theta) r\,dr\,d\theta = \frac{1}{(2n+1)} \delta_{nm'} \delta_{nm}$$

where 1/(2n+1) : normalization constant.
Orthogonality to express any function f(r,θ) on circle as a sum of Zernike functions

$$f(r,\theta) = \sum_{n=0}^{\infty} \sum_{m=-n}^{n} a_{nm} Z_n^m(r,\theta)$$

2D Zernike analysis can be extended to apply to 3D material property distribution
3D method: Use angular variable with the Zernike radial function

where $Z_{nl}^m = R_{nl}(r) Y_l^m(\theta,\phi)$: radial Zernike function with spherical harmonics

$$Y_l^m(\vartheta,\phi) = N_l^m P_l^m (\cos(\theta))e^{im\theta}$$

$$N_l^m = \sqrt{\frac{2l+1}{4\pi}\frac{(l-m)!}{(l+m)!}} \quad , \quad P_l^m: \text{Legendre functions}$$

with $l \leq n$, $m \leq l$ and (n-1) must be even also apply to the 3D Zernike
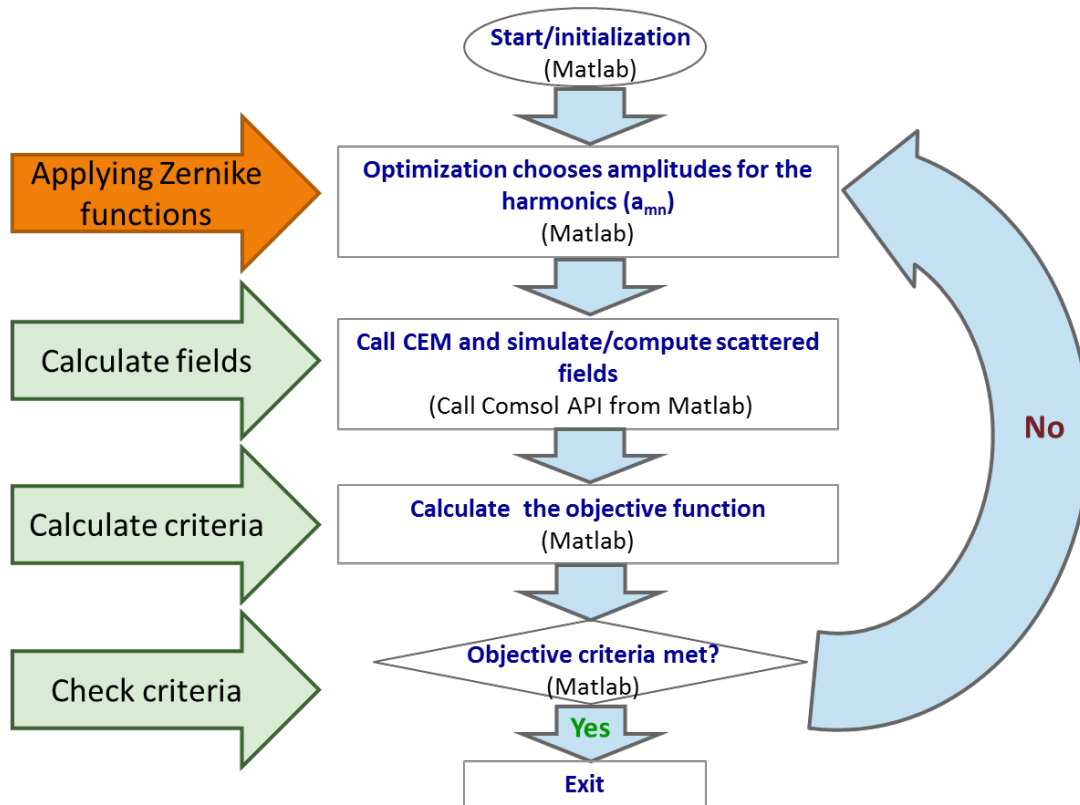
Figure 3: Optimization Process Flow Chart
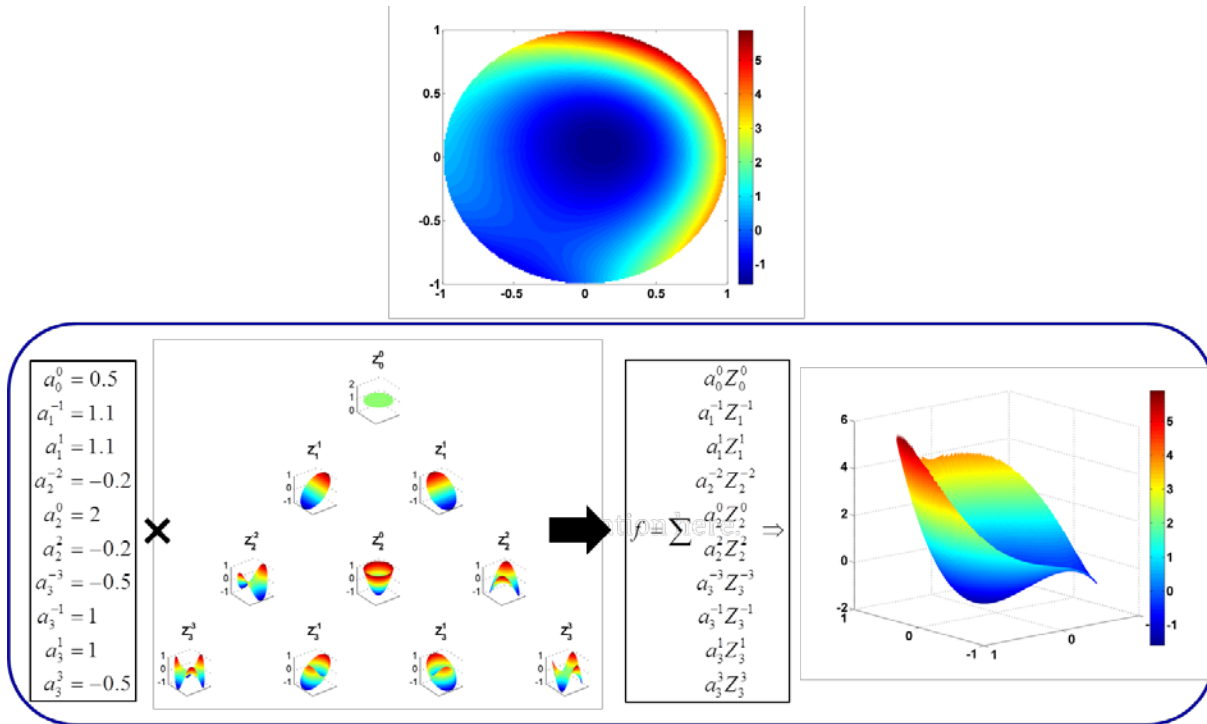
Figure 4: First 10 Zernike Functions

What follows are a few practical examples of how such a optimization process using Zernike bases function can be used. First we start off with the goal of reducing the scattering cross-section of given object (cylinder).The scattered electric field from plane wave incident at 350° without metamaterial shell as shown below.
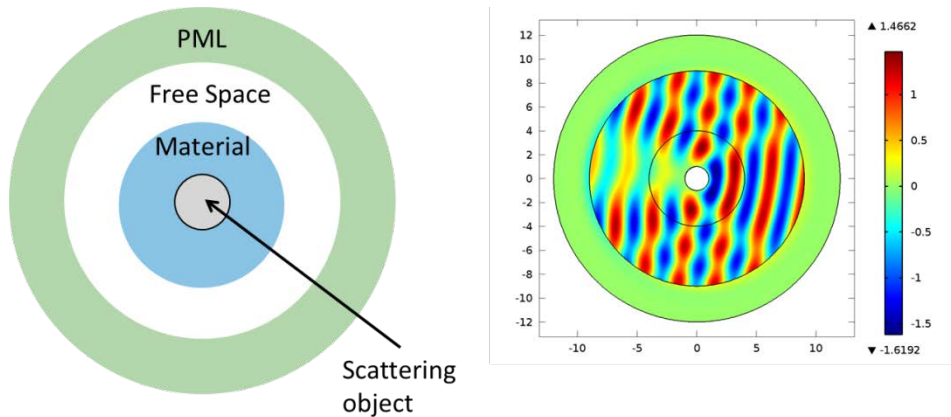
Figure 5: Scattering from a Cylindrical PEC

The material parameters in $r < R_2$ are mapped into $R_1 < r < R_2$ using the following transformation

Approved for public release; distribution is unlimited.
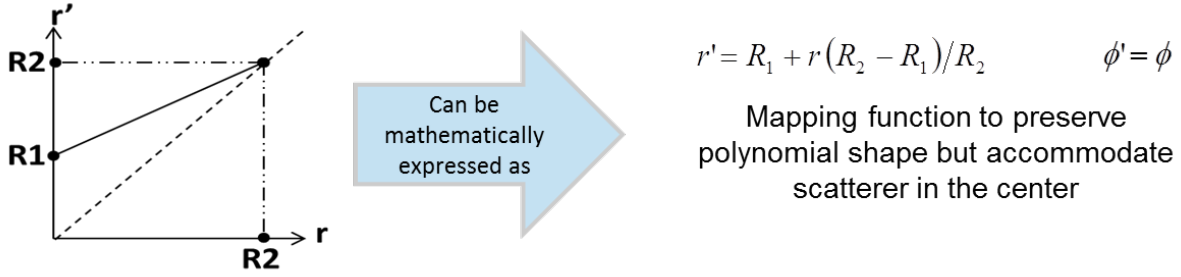
Figure 6: Mapping Function/Transformation

The resulting polynomial Zernike plot is shown below where a solid single mode is mapped to create a central discontinuity using the mapping function.
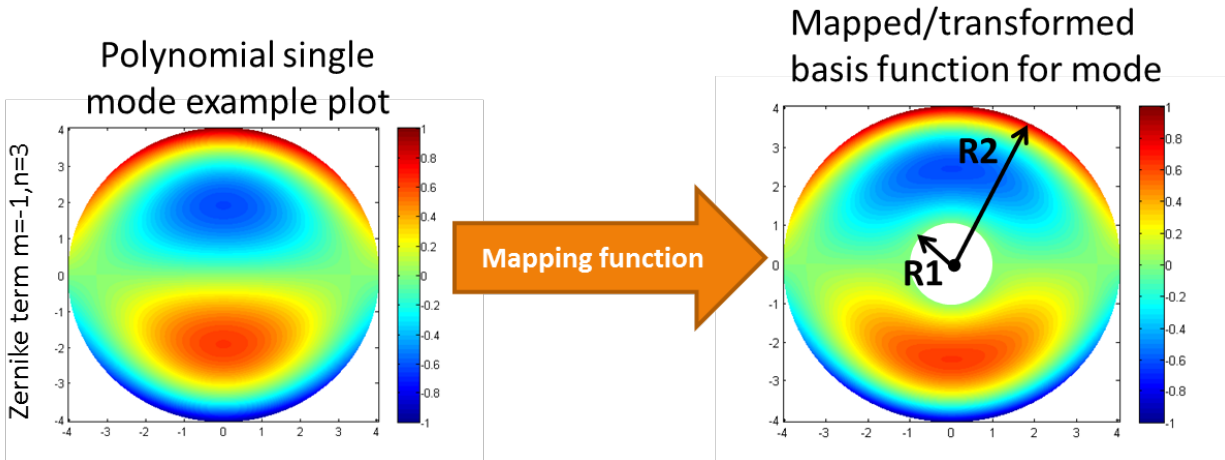
Figure 7: Mapping Function as Applied to a Single Zernike Mode

To minimize scattering cross-section and total scattered field we define the objective function, calculate fields using full wave EM models and optimize material parameters using Zernike moments. Here the objective function to be minimized is the total scattered field,

$$\text{Scattering cross-section, } \sigma_{scat} = \frac{|E_{scat}(\phi)|^2 \cdot 2\pi r}{|E_{inc}(\theta)|^2}, \text{ Total scattered field, } \sigma_{total} = \sum_{j=0}^{n}\sum_{i=0}^{m} \sigma_{scat}(\phi_i, \theta_j)/m$$

where E_{scat}: Scattered field, E_{inc}: Incident field, θ: incident angle, r, ϕ: cylindrical coordinates, $0 \leq \phi \leq 2\pi, 0 \leq \theta \leq 2\pi$

In this example, we start with a cylinder (radius=0.125λ; ε=3) scattering a plane wave incident at 350°. The scattered electric fields and scattering cross-section are calculated as a baseline before an optimized metamaterial shell is placed around the object to reduce scattering.
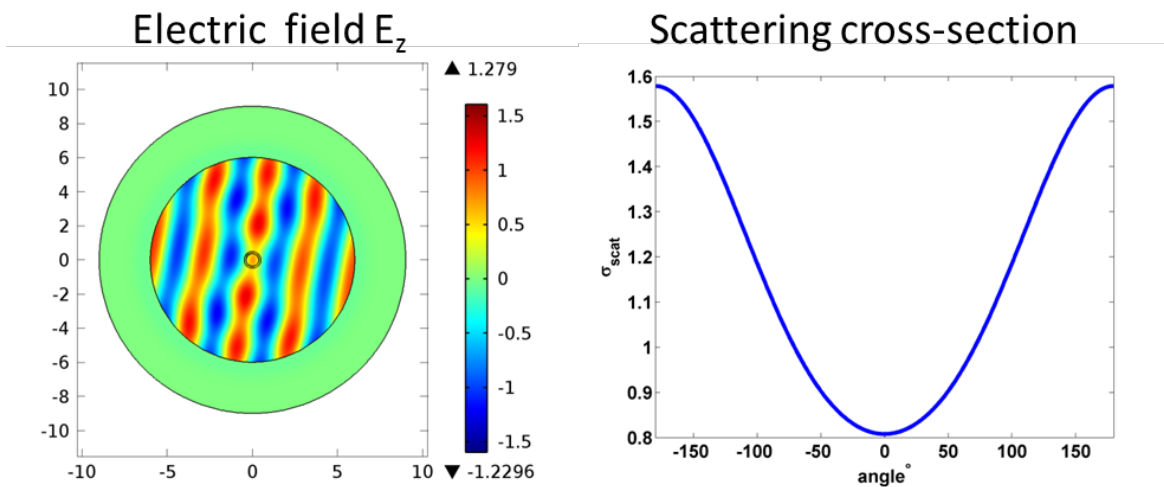
Figure 8: Baseline Scattering from a Dielectric Cylinder

What follows are two solutions obtained using the process described above showing of how the scattering from the dielectric cylinder can be reduced using a thin optimized metamaterial shell.
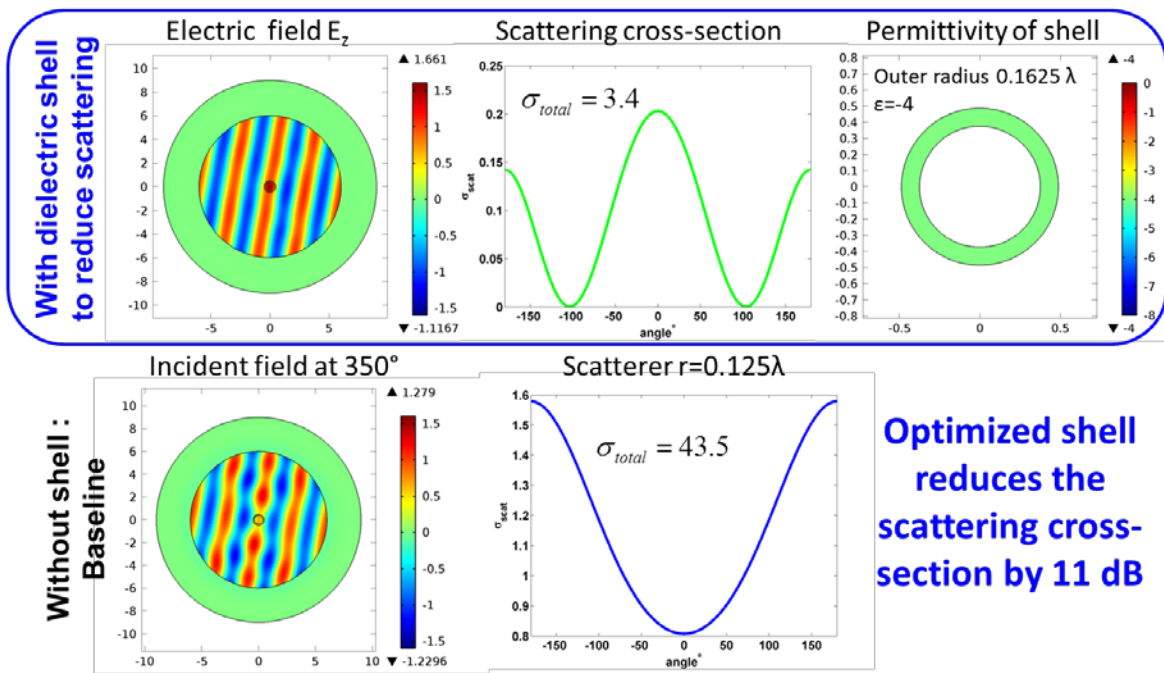
Figure 9: Constant Dielectric Metamaterial Shell of Negative Permittivity
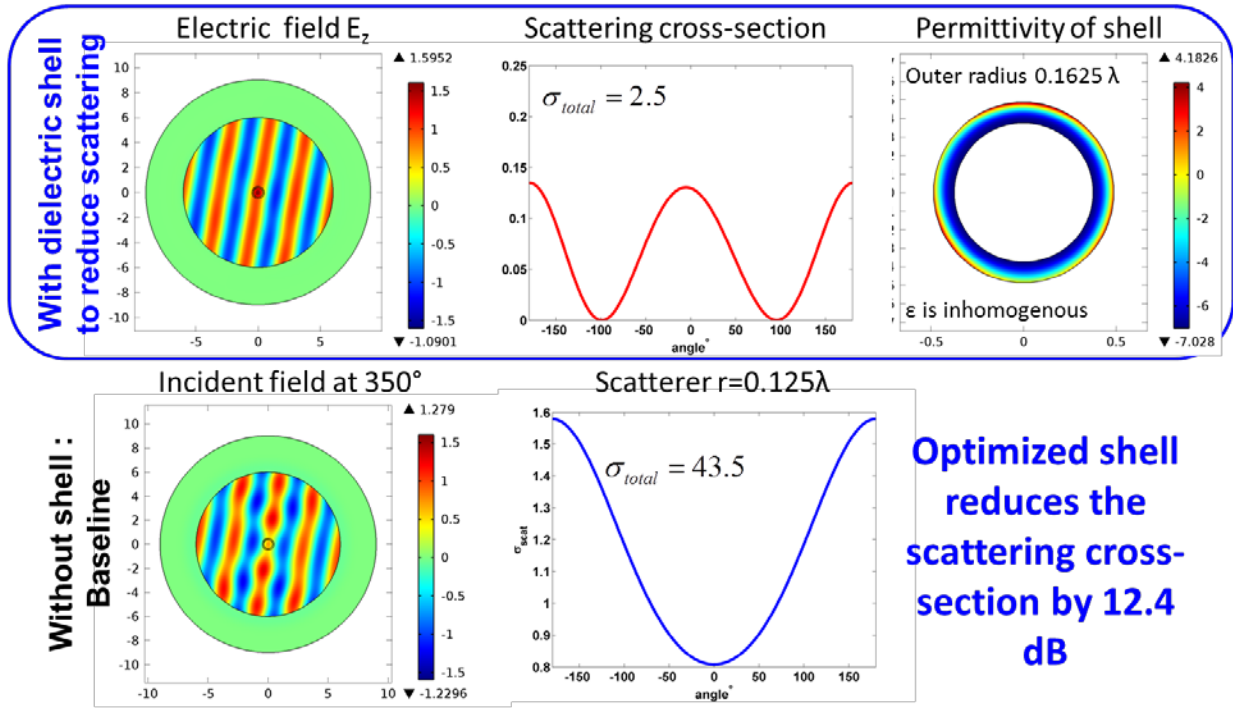
Figure 10: Inhomogeneous Dielectric Metamaterial Shell

Next we optimize a structure with a larger shell that relies on guiding the waves around the scatterer. Here 4 Zernike moments were used to optimize and represent the spatial distribution of μ_r

$$\mu_\phi = 1, \; \varepsilon_z = \left(\frac{R_2}{R_2 - R_1}\right)^2, \; \mu_r = \left(\frac{r - R_1}{r}\right)^2$$

To compare the results with prior work we starting with the equations of an approximate cloak: Optimize ε_z and μ_r while holding $\mu_\phi = 1$. In this example, we start with a cylinder (radius=$\lambda/3$; PEC) scattering a plane wave incident at 350°. The scattered electric fields and scattering cross-section are calculated as a baseline before optimized metamaterial shell is placed around the object to reduce scattering.
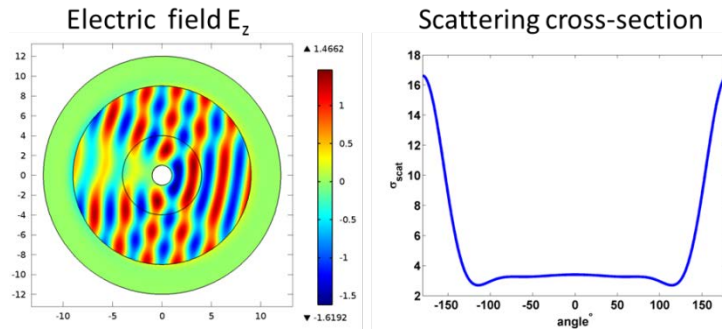
Figure 11: Scattering Cross Section from PEC of Radius=$\lambda/3$

We use the basis function optimization to design a shell with inner radius λ/3 and outer radius 4λ/3 that reduces the cross-section of a scattering cylinder. The resulting material parameters are shown below
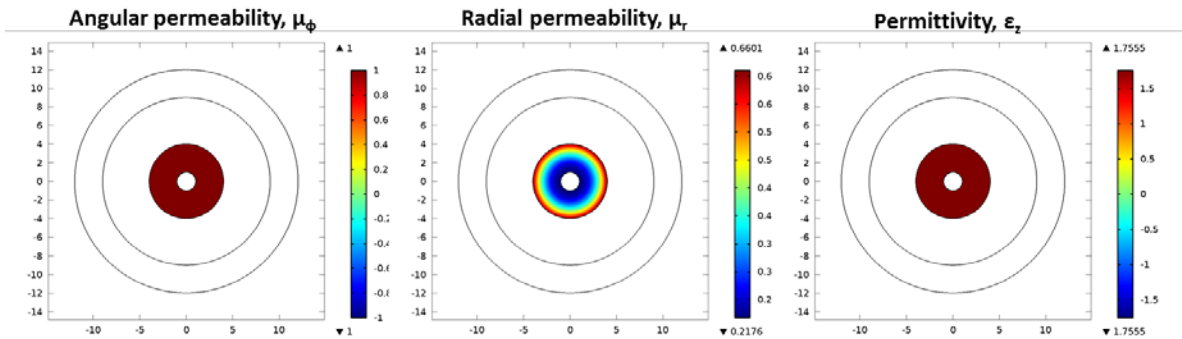
Figure 12: The Material Parameters Obtained by Optimization for the Metamaterial Shell
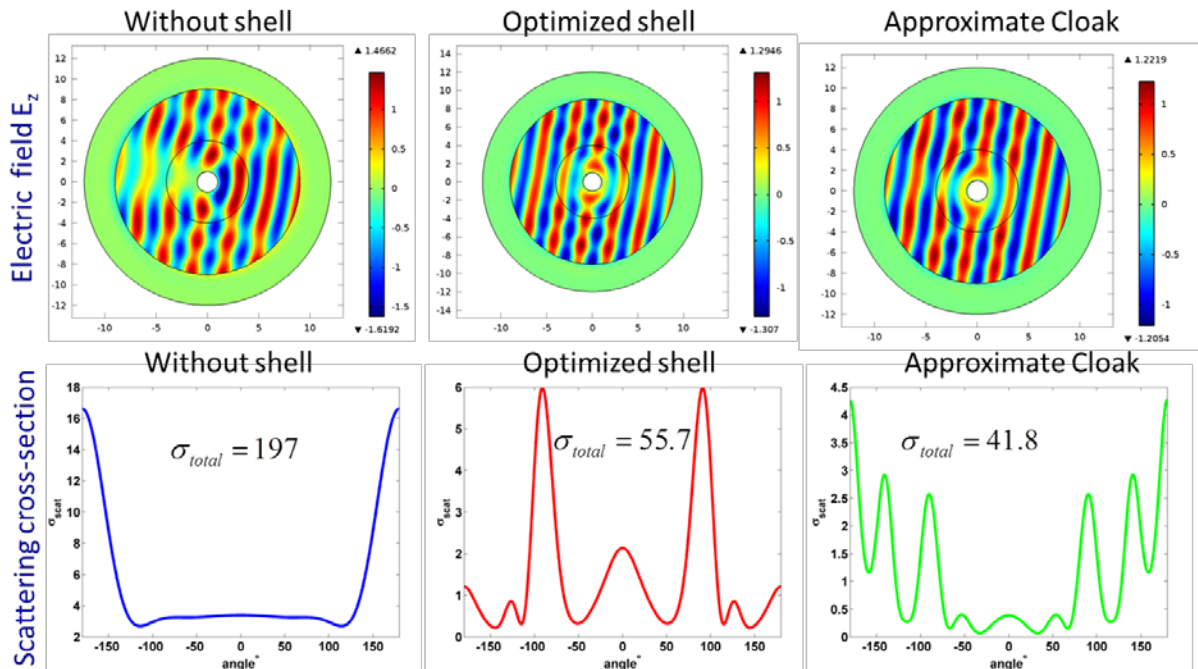
Figure 13: Results and Comparisons of Scattering for Approximate Cloak and Optimized Cloak

2.2.3   Third Year Summary

During 2014 this subtask consisted of two major objectives: demonstration of a passive optimized component (lens) and inclusion of active source into the passive transformed space for a cohesive combined transformation. We use the source transformations approach to manipulate antenna arrays such that the physical location/shape is dictated by the system (e.g. wing/fuselage) and the electromagnetic performance is defined by the application. Numerical

simulations how an array with sources arranged in a circular manner can be surrounded by a transformation optics medium so that it can be made to receive and radiate as if it were a linear array of uniformly spaced elements and vice versa. We have finished setting up, configuring and coding the software problem in Matlab and computational electromagnetic solvers (Comsol) for full-wave electromagnetic simulation models where the shape of individual sources was changed using Source Transformation Optics (STO). This first set of simulations provided solutions to the ideal case and valuable information into the upper bounds defined by the physics of the problem. This information will be used in optimization routines to develop appropriate approximate Transformation Optics (TO) media with practical parameters that can be fabricated and measured using standard testing procedures.

The media transformation equations for the source transformation of sources ar-ranged in a circular manner can be surrounded by a transformation-optics medium so that it can be made to receive and radiate as if it were a linear array of uniformly spaced elements and vice versa were derived. However, the expressions relating the original coordinates to the desired coordinates do not have inverse expressions. Hence, the summation notation representation of the problem does not have a direct solution. We use properties of the Jacobian matrix and matrix algebra to formulate the expression for the transformed tensors. This approach does not require an explicit expression for the inverse relationships of the coordinates. In the following expressions are used to transforming a uniform array of line sources to a non-uniformly spaced circular array of line sources.

$$x(r', \phi', z') = a(r') \cos \phi'$$
$$y(r', \phi', z') = b(r') \sin \phi'$$
$$z(r', \phi', z') = z'$$

where

$$a(r') = \frac{R_2}{R_2 - R_1}(r' - R_1), \quad R_2 < r' < R_1$$

$$b(r') = \frac{R_2 - \frac{d}{2} - \delta}{R_2 - R_1}(r' - R_1) + \frac{d}{2} + \delta, \quad R_2 < r' < R_1$$

As there are no inverse relationships of the forms

$$r' = r'(x, y, z)$$
$$\phi' = \phi'(x, y, z)$$
$$z' = z'(x, y, z)$$

the summation notation and explicit formulations for the tensor elements cannot be used. Instead, we rely on the properties of the Jacobian matrix A where A is defined below

$$\epsilon'_{r\phi z} = \frac{A\epsilon_{xyz}A^T}{\det A} = \frac{A\epsilon_0 I A^T}{\det A}$$

where $\epsilon_0 I = \epsilon_0 \delta^{ij}$ is the isotropic and homogeneous material tensor. The Jacobian matrix A is explicitly expressed in terms of the derivatives of as:

$$A = \frac{\partial(r', \phi', z')}{\partial(x, y, z)} = \left[\frac{\partial(x, y, z)}{\partial(r', \phi', z')}\right]^{-1} = \begin{bmatrix} \frac{\partial x}{\partial r'} & \frac{\partial x}{\partial \phi'} & \frac{\partial x}{\partial z'} \\ \frac{\partial y}{\partial r'} & \frac{\partial y}{\partial \phi'} & \frac{\partial y}{\partial z'} \\ \frac{\partial z}{\partial r'} & \frac{\partial z}{\partial \phi'} & \frac{\partial z}{\partial z'} \end{bmatrix}^{-1} = B^{-1}$$

the permittivity can be determined from

$$\epsilon'_{r\phi z} = \frac{A\epsilon_{xyz}A^T}{\det A} = \frac{B^{-1}\epsilon_{xyz}(B^{-1})^T}{\det B^{-1}}$$

One advantage of using this approach is that the resulting expression will be in terms of the primed variables. A disadvantage is that the perspective of the differential field behavior due to differential material changes is lost. Also, the matrix algebra does become quite tedious. The Jacobi matrix A is first calculated from B^{-1} where

$$B = \begin{bmatrix} \frac{\partial x}{\partial r'} & \frac{\partial x}{\partial \phi'} & \frac{\partial x}{\partial z'} \\ \frac{\partial y}{\partial r'} & \frac{\partial y}{\partial \phi'} & \frac{\partial y}{\partial z'} \\ \frac{\partial z}{\partial r'} & \frac{\partial z}{\partial \phi'} & \frac{\partial z}{\partial z'} \end{bmatrix} = \begin{bmatrix} \frac{\partial a(r')}{\partial r'}\cos\phi' & -a(r')\sin\phi' & 0 \\ \frac{\partial b(r')}{\partial r'}\sin\phi' & b(r')\cos\phi' & 0 \\ 0 & 0 & 1 \end{bmatrix} = \begin{bmatrix} b_{11} & b_{12} & 0 \\ b_{21} & b_{22} & 0 \\ 0 & 0 & b_{33} \end{bmatrix}$$

and

$$b_{11} = \frac{R_2}{R_2 - R_1}\cos\phi'$$

$$b_{12} = -\frac{R_2}{R_2 - R_1}(r' - R_1)\sin\phi'$$

$$b_{21} = \frac{R_2 - \frac{d}{2} - \delta}{R_2 - R_1}\sin\phi'$$

$$b_{22} = \left[\frac{R_2 - \frac{d}{2} - \delta}{R_2 - R_1}(r' - R_1) + \frac{d}{2} + \delta\right]\cos\phi'$$

$$b_{33} = 1$$

The matrix inverse can be computed using Cramer's Rule. The result is not shown here, but the resulting elements of the relative permittivity tensor expressed in Cartesian coordinates are

$$\epsilon'_{xx} = \frac{4R_1^2\left(\frac{R_2}{R_2-R_1}\right)^2 y^2 + d^2 x^2 + 4d\delta x^2 + 4\delta^2 x^2}{2(d+2\delta)\left(\frac{R_2}{R_2-R_1}\right)^{3/2}\sqrt{x^2+y^2}}$$

$$\epsilon'_{xy} = \epsilon'_{yx} = \frac{\frac{R_2}{R_2-R_1}x^2(d+2\delta)\left[\frac{y}{\left(\frac{R_2}{R_2-R_1}\right)^2 x} - \frac{2R_1 y\left(4x^2y^2 + 2x^4 + 2y^4 - 2R_1 y^2\sqrt{x^2+y^2}\right)}{x^3(d+2\delta)^2 \cdot \sqrt{x^2+y^2}}\right]}{2^{\cdot 3/2}\sqrt{x^2+y^2}}$$

$$\epsilon'_{yy} = \frac{\frac{R_2}{R_2-R_1}x^2(d+2\delta)\left[\frac{y^2}{\left(\frac{R_2}{R_2-R_1}\right)^2 x^2} + \frac{4\left(2x^2y^2 + x^4 + y^4 - R_1 y^2\sqrt{x^2+y^2}\right)^2}{x^4(d+2\delta)^2 \cdot (x^2+y^2)}\right]}{2^{\cdot 3/2}\sqrt{x^2+y^2}}$$

$$\epsilon'_{zz} = \frac{\frac{R_2}{R_2 - R_1}x^2(d+2\delta)}{2^{3/2}\sqrt{x^2+y^2}}$$

Lastly, the sources are also transformed using the Jacobian matrix. The steps are not shown here, but the following graphs show the results using COMSOL Multiphysics.
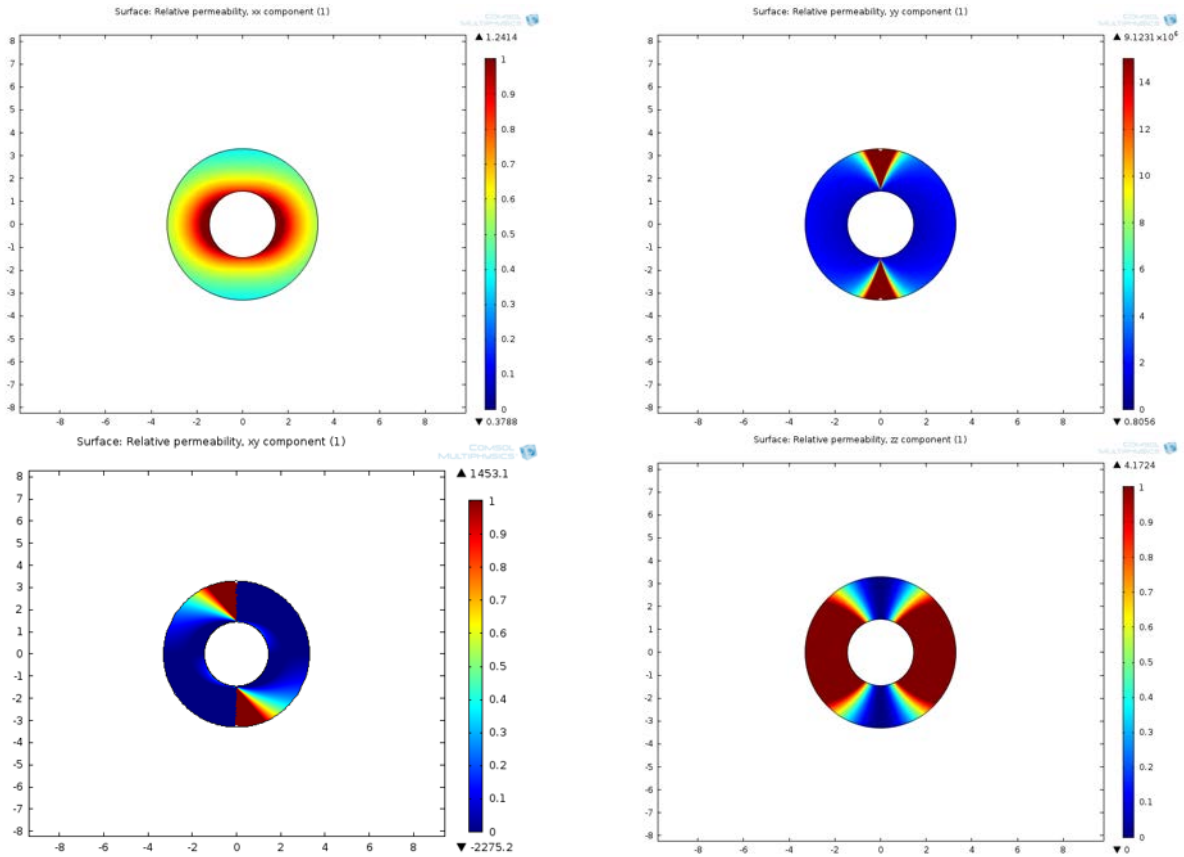
Figure 14: Relative Permeability (same as relative permittivity). Due to Symmetry of Tensor, Only Four Elements are Shown. Upper Left: μ_{xx}, ϵ_{xx}; Upper Right: μ_{yy}, ϵ_{yy}; Lower Left: $\mu_{xy} = \mu_{yx}, \epsilon_{xy} = \epsilon_{yx}$; Lower Right: μ_{zz}, ϵ_{zz}
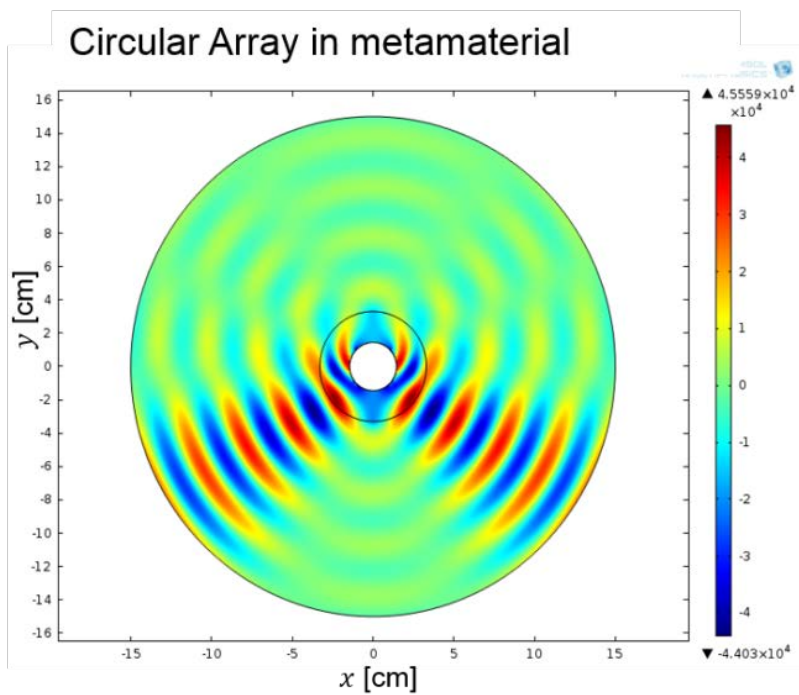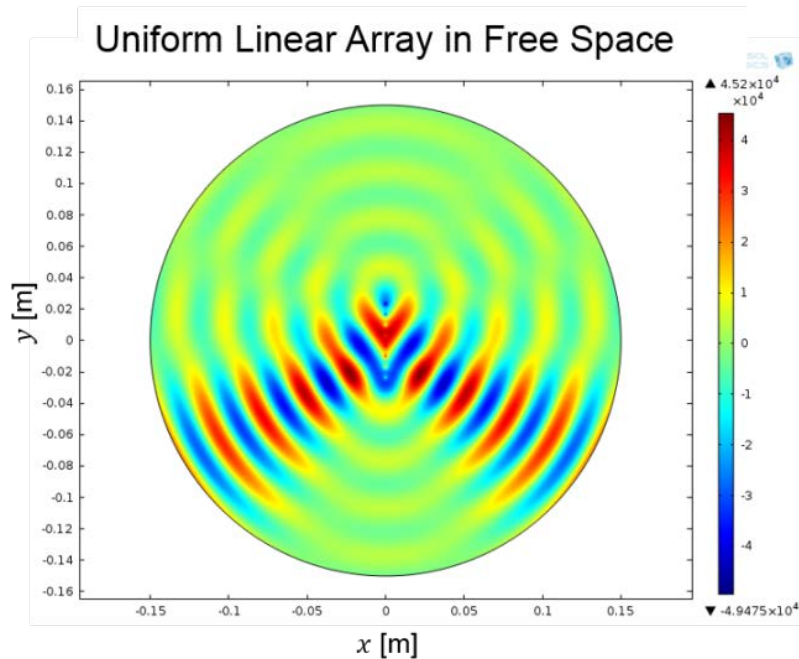
Figure 15 Radiation Patterns. (Top) Uniform Linear Array in Free Space. (Bottom) Circular Array with Thick Coating

2.3 Conclusions and Future Work

In summary, we specifically addressed the following:

- Scattering inverse problem: Conducted full wave simulations using Comsol and Matlab program with optimization routines to include basis function coefficients
  - Small dielectric scatterer
  - Approximate cloak
- Radiation inverse problem exploration
  - Started with 3 source known example
  - Helped research idea on optimizing material parameters using basis functions to achieve desired far-field pattern

Next, we suggest the following research direction: (i) Derive analytical solutions based on form-invariant Maxwell's equations in the STO framework for the transformed sources as well as TO media; (ii) Develop in-house Matlab code to simulate the passive TO case operation that can provide insight into the wave propagation in the designed media; (iii) Perform finite element method (FEM) based simulations using software packages such as Comsol® to predict the behavior of untransformed and transformed arrays; and (iv) Compare results from (iii) with respect to EM fields and far-field patterns to demonstrate the efficacy of the approach.

3 Subtask 2: Antennas Operating in Close Proximity to a Textured Surface

In this work a new method to control the interaction between antennas and nearby objects is proposed. It involves the use of a thin textured surface similar to a high-impedance layer that is wrapped around the objects that are located in close proximity of the antenna (such as ground planes, various platforms, etc.). The textured surface acts as a "diffuser" spreading the reflected fields from the close objects and thereby reduces the power otherwise directed in specular reflections. This method allows reducing the profile of antennas working in close proximity to various objects.

3.1 Introduction

The requirement for low profile antennas that are conformal to large and finite bodies is not new. Typical examples are antennas mounted on an aircraft pod (Figure 16a). The desire is to minimize the profile of these pods, which would bring the antennas very close to the aircraft body (Figure 16b). The aircraft body can be of any size, shape or materials, but when the antenna is brought too close to it, the performance of the antenna will, in most cases, deteriorate. Antennas operating in the close proximity of finite bodies present significant deficiencies, due to the strong interaction between the two. Any energy emanating from the antenna undergoes a reflection from the object present in close proximity, resulting in distortion of the radiation pattern. Edge effects from the finite object also contribute to beam degradation. Squint in the main beam, increased cross-polarization, and high-level sidelobes are only some of the negative effects of this interaction, which impose constraints on the design of a low profile antenna system that almost blends with the finite body.

Figure 16 (a) Traditional High-Gain Antenna in a Pod; (b) Low Profile Antenna in a Pod with a. Platform, b. Pedestal, c. High Gain Antenna, d. Radome, e. the Direction of the Main Beam

This work describes an approach to address the distortion of the pattern due to the interactions with the finite body. In this approach, a textured periodic surface is used to reduce the interaction such that the negative effects are largely eliminated over a certain frequency band. The only positive effect is the increased directivity resulting from the array of the antenna with its image.

3.2 Problem Definition

The proposed test case is shown in Figure 17. An end-fire (low-profile) dielectric polyrod antenna operates in free space. The details of the antenna geometry are given in Table 1. For

reference, Figure 18 shows its radiation pattern in the elevation (xy) plane. The free space radiation pattern, as expected, is symmetric, with a well-behaved main beam and a gain of 13.4 dB at 32GHz.

Table 1 Antenna Design Geometry

PEC ground size	217x217mm (23x23 λ @ 32GHz)
Antenna Length	29.25mm (~3 λ @ 32GHz)
Distance from the PEC to the axis of the antenna	8.635mm (0.92 λ @ 32GHz)
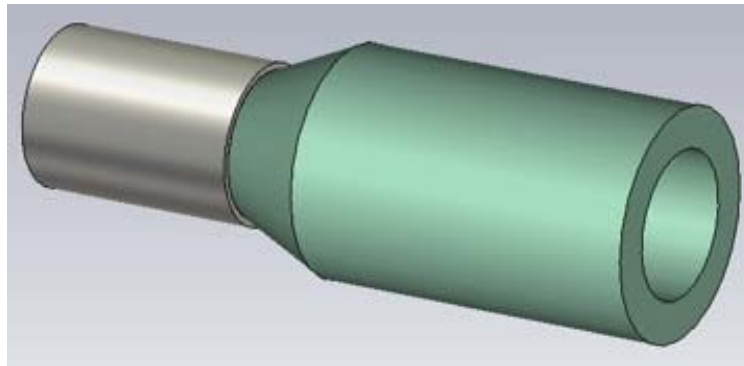
Figure 17 A Waveguide Fed Multimode Dielectric Polyrod Antenna
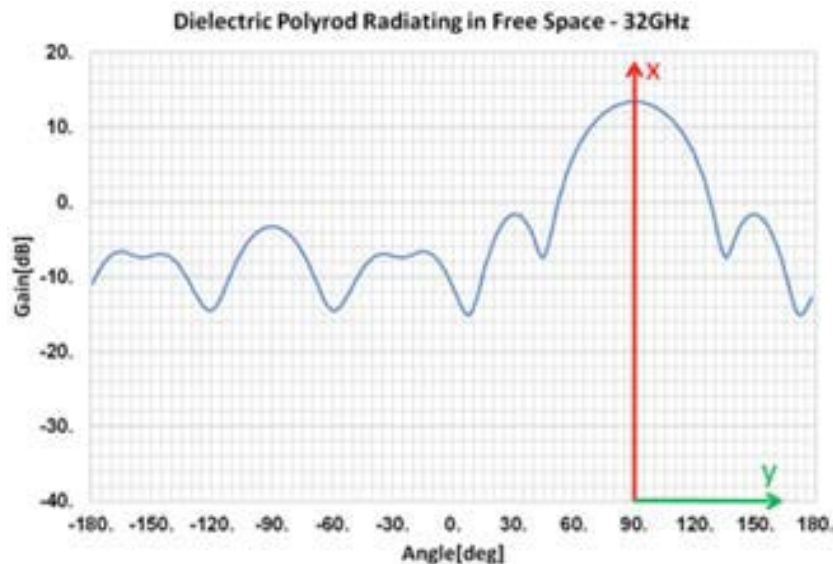
Figure 18 The Radiation Pattern in the XY-Plane

Next, the antenna is positioned in close proximity to a flat PEC object. While image theory provides some insight into the problem, due to the complexity of the equivalent sources (both electric and magnetic) required to adequately represent the antenna and the finiteness of the PEC object, the image theory may be only partially be used to understand the phenomenology.

19

Since the interaction occurs in the reactive region of the antenna, none of the other analytical methods are applicable. Therefore, the use of numerical full-wave methods is required (in this case Microwave Studio by CST and HFSS by Ansoft were used).

The results of the Microwave Studio analysis of the polyrod antenna are shown in Figure 19. Figure 19 shows a. the elevation pattern of the polyrod located at 0.92λ above an infinite PEC ground plane and b. the elevation pattern at the same height above a rectangular finite PEC ground plane. As expected, when placed above an infinite ground plane, the maximum of the main lobe is in the endfire direction (x-axis). The differences between the finite PEC ground and the infinite PEC ground are evident: in addition to the nulls shown for the infinite PEC case, the beam is squinted by about 17 degrees (~50% of the 42 degree beamwidth) and many additional ripples are noticed in the pattern. Although the finite ground is 23λ by 23λ (which can be considered an electrically large ground), the edge effects are still significant.
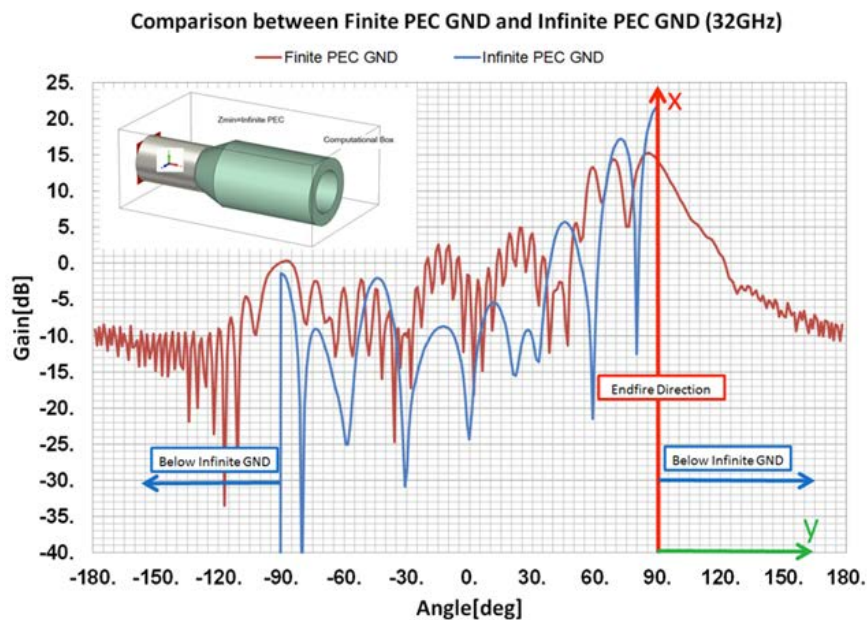
Figure 19 A Comparison Between the Elevation Radiating Patterns When the Polyrod is Operating in the Proximity of an Infinite PEC Ground and a Finite PEC Ground

3.3   The New Concept for Pattern Reconstruction

A number of techniques have been used in the past to reduce these unwanted effects:

1. Using absorbing materials on the edges of the finite objects. This significantly affects the efficiency of the radiator.

2. Using serrations on the edges of the finite objects. This significantly increases the size and complexity of the antenna system.

3. Shaping the edges of the finite objects. This method is applicable only for electrically large bodies.

The method proposed here attempts to diffuse the specular reflections from the scattterer. The effect of diffusion is achieved by mode conversion of the incident wave. The finite object is

covered by a textured surface that has the capability to reflect and convert an incident plane wave into a combination of higher order modes. Specifically, assuming that a textured surface is a periodic structure that operates in the grating lobes regime, the characteristics of the unit cell are such that for any incident plane wave, less power is delivered to the dominant mode, and more power is delivered to the higher order modes. This corresponds to a lower level specular reflection pattern and a higher envelope of minor reflection sidelobes.

For example, Figure 20 shows a textured surface unit cell called higher order mode diffuser. Note. The geometry looks similar to a typical EBG unit cell, however the functionality is completely different. The only thing in common between the EBG unit cells and this higher order mode diffuser unit cell is the fact that they are both periodic structures. The dimensions, the shape and the frequency band of operations are such that the unit cell, for any incident plane wave it supports and excite higher order modes. Figure 21 shows the electric field distributions for some of the higher order modes.
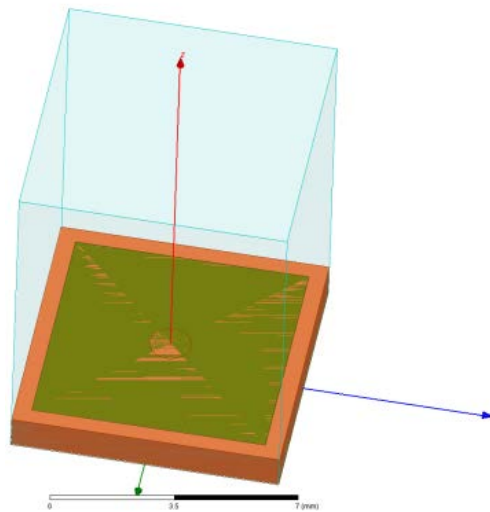
Figure 20 The Higher Order Mode Diffuser Unit Cell
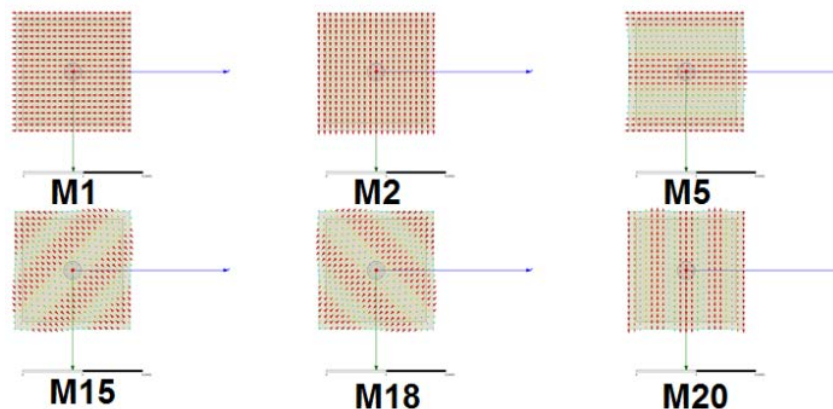
Figure 21 The Field Distributions of Various Higher Order Modes

The analysis of this particular unit cell shows that for a normal incidence, the power delivered to mode 0 (specular reflection) is somewhat reduced and is comparable to the level of power delivered to mode 6 and 7 (Figure 22). This means that the power delivered to the main reflection beam is reduced. The effect is significant at 32 GHz, where the power delivered to mode 6 and 7 is comparable to the power delivered to mode 0. The effect is negligible at 40 GHz, there even thought 'some' power is delivered to mode 6 and 7, the level is not high enough to produce the desired effect. As shown in Figure 23, the desired effect is achieved in three frequency bands; in all cases the reduction in power of the dominant mode is higher than 1dB. Considering that the main beam destruction noted in Figure 3 is the result of the superposition of a direct wave and a reflected wave, the attenuation of the reflected wave by more than a 1 dB can avoid the destructive superposition between the direct wave and a reflected wave. This way, the detrimental impact of the finite objects is considerably reduced.
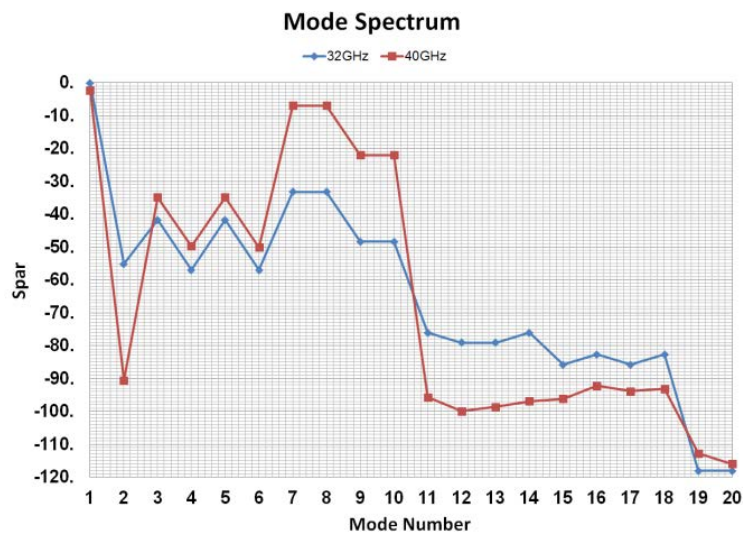
Figure 22 The Power Delivered to the Various Modes at 32 GHz and 40 GHz
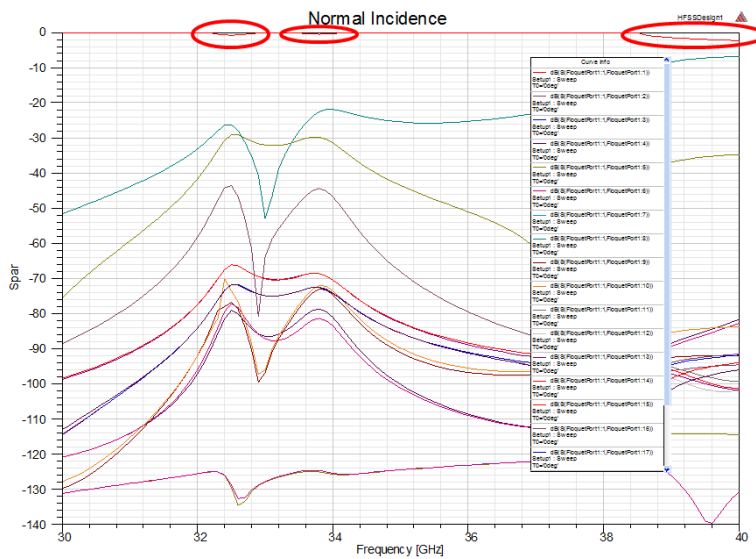
Figure 23 The Return Loss of the First 20 Modes

This principle was applied to the waveguide fed multimode dielectric polyrod antenna located over the finite ground mentioned above. This time, the ground was covered by an array of unit cells described above (Figure 24).
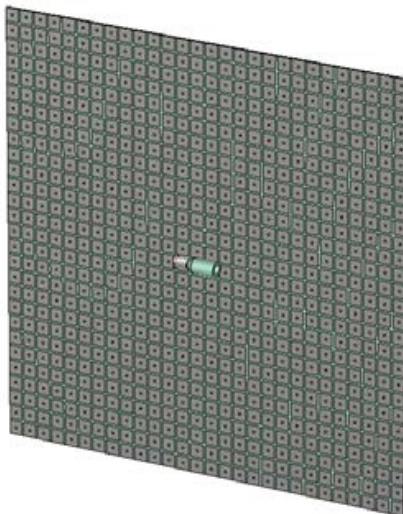
Figure 24 The Dielectric Polyrod Located at 0.92λ above a Finite Textured Surface Backed by a PEC Ground

Figure 25 shows the elevation radiation patterns of this combination at 32GHz, compared to the same pattern in the absence of the textured surface and the pattern of the element operating in free space. As shown in Figure 25, in the presence of the textured surface the polyrod antenna radiation pattern is again, well behaved. No ripples are noticed in the main beam and the sidelobe levels are close to the ones for the free space case. The presence of the ground is noted by the

gain in directivity as predicted by the image theory. As mentioned before, the squint is due to the finiteness of the textured surface and is not addressed at the moment by this technique.
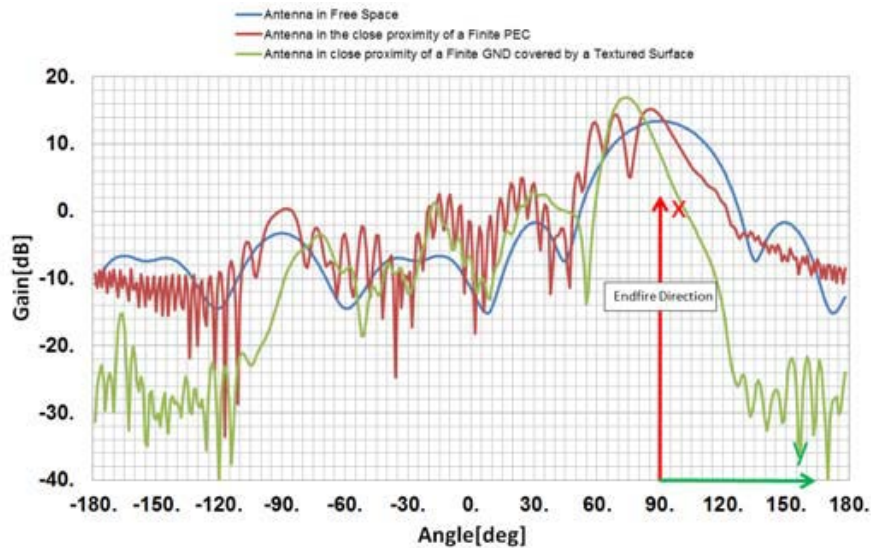
Figure 25 Elevation Patterns for the Dielectric Polyrod in Free Space, Located at 0.92λ above a PEC Ground and Located at 0.92λ above a Finite Textured Surface Backed by PEC Ground

3.4   Conclusion

A new method for improving the radiation patterns of antennas operating in close proximity of finite objects was presented. The results are promising and further investigation is required, mainly regarding the bandwidth capabilities of this concept and the robustness of the method. The inherent edge effects might be reduced using a non-uniform textured surface with specific characteristics (such as surface impedance and diffraction coefficients), which may require different values for different sections of the surface. This is a topic for further investigations.

4 Subtask 3: Topics in Transformation Optics and Metamaterials

Metamaterials and transformation optics are two research topics that are of significant importance in electromagnetics. Transformation optics allows us to find the required constitutive parameters associated with spatial coordinate transformation. Metamaterials, which can be described as synthesized materials with constitutive parameters that can be defined macroscopically to a certain practical extent, have given rise to a branch of electromagnetics in its own rights and have provided a conceptual means for realizing the complex media resulted from TO.

4.1 Objective

In recent years, transformation electromagnetics has found potential applications in propagation, waveguiding, scattering, and radiation. For antenna applications, using transformation techniques, one can transform bulky antennas to low profile ones. In general, the resulting medium will be both inhomogeneous and anisotropic. In this section, we proposed a spherical core-shell structure which can achieve arbitrarily large directivity. We investigated the problem by finding the transformed constitutive tensors and solving the equivalent problem in the core-shell configuration. Using the Ricatti-Bessel functions, we can represent the field components with Debye potentials and subsequently solve for the fields in all regions. We applied the formulation to several cases of dipole arrays within the shell, corresponding to both free-space and half-space problems in the virtual space. Overall, the calculation demonstrated that the formation of virtual aperture is indeed theoretically possible and the effects of loss on the number of available spherical harmonics and directivity are investigated.

4.2 Technical Summary

4.2.1 Introduction

Transformation electromagnetics has received a lot of interests in recent years. It has found potential applications in several major areas of electromagnetics: propagation, waveguiding, scattering, and radiation. Using transformation electromagnetics, it is possible to manipulate the electromagnetic waves to achieve novel effects. For propagation and waveguiding, transformed structures allow waves to propagate and bend without suffering from reflections. Regarding scattering, both monostatic and bistatic scattering can be reduced. In this section, we are primarily interested in antenna applications. For antenna applications, transformation techniques, including compression and conformal mapping, allow the transformation of bulky antennas to low profile ones. For example, consider the parabolic antenna in Figure 26 The parabolic antenna on the left with isotropic medium can be transformed into a low profile antenna on the right [4]. The resulting medium will be both inhomogeneous and anisotropic.

For the horn antenna shown in Figure 27, the structure on the left with isotropic medium can be transformed into a smaller package with compression. The resulting medium in this case is anisotropic but can be homogeneous. This has also found potential applications for decreasing the spacing between antennas and ground planes to reduce the typically quarter-wavelength

distance. The resulting medium, compressed in the normal direction, will have constitutive parameters: $\varepsilon = \hat{x}\hat{x}a\varepsilon_1 + \hat{y}\hat{y}a\varepsilon_1 + \hat{z}\hat{z}(1/a)\varepsilon_1$ and $\mu = \hat{x}\hat{x}a\mu_1 + \hat{y}\hat{y}a\mu_1 + \hat{z}\hat{z}(1/a)\mu_1$, where the original medium has isotropic permittivity ε_1 and permeability μ_1. The thickness is reduced by a factor of **a**. Notably, the idea of using materials with high permittivity or high permeability can be thought of as an approximation of the ideal transformed case. Such an approximation will naturally have good performance for radiation in the broadside direction, but for other directions equivalence of the complex fields in the entire region of interest with respect to the uncompressed case can only be obtained via the inclusion of effective anisotropy, even though this specific transformation is not unique.

Whether we are transforming a parabolic reflector or achieving low profile via simple compression, the effective aperture does not increase without space projection. This can be understood from the previous idea of "perfect lens" [5], which has been reinterpreted using coordinate transformations [6]. Effectively, space projection can create or cancel out space and maintain the perfect matching between the media.
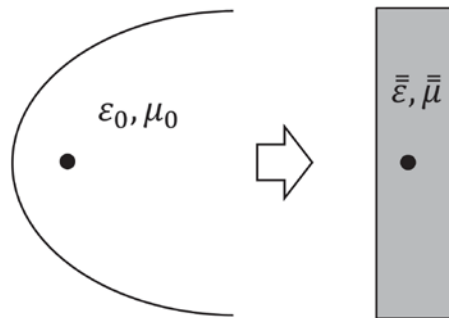
Figure 26 Transformation of a Parabolic Antenna into a Low Profile Antenna. Left: Original Space. Right: Transformed Space
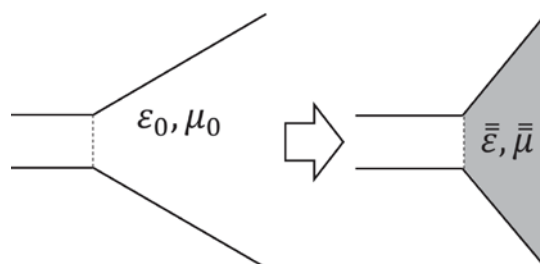
Figure 27 Transformation of a Horn Antenna. Left: Original Space. Right: Transformed Space

In this subtask, we present a layered spherical structure that is able to form a virtual aperture in empty space by applying the appropriate space projection. Subsequently, the radiated fields will be emitted as if they are from the virtual aperture. Reducing the dimensions of radiators is always of great interest in the antenna engineering community. It is well known that there is no mathematical upper limit to the directive gain of an antenna of a given size [7]. However, there

Approved for public release; distribution is unlimited.

still lacks a general design capable of producing arbitrarily large directivity. With our proposed model, any arbitrarily large directivity can be theoretically achieved. The underlying concept has been demonstrated in [8]. Here we formulate the problem with a difference in terms of the potentials used to represent the fields. In addition, we also analyze the limit of the achievable farfield resolution.

In the following sections, the formulation for the transformed constitutive parameters and the solution to the radiation problem will be given and we will look at the fields and farfield radiation patterns for different cases and explore the resolution limit. Whereas many problems in transformation electromagnetics can be solved numerically via electromagnetics software packages, it is hoped that the analysis here will provide basis for future comparisons, allow us to analyze the effect of loss, and provide some insights to the resolution limit.

4.2.2 Formulation

In this section, we will set up the problem in such a way that instead of using coordinate transformations to calculate the fields, we will be solving a transformed version of the original problem in the physical space. The transformation will result in a shell whose medium will be radially inhomogeneous and anisotropic. We will be using the time-harmonic convention $e^{-i\omega t}$ throughout this section. The time harmonic Maxwell's equations are:

$$\nabla \times \overline{E} = i\omega\overline{B} , \tag{1}$$

$$\nabla \times \overline{H} = -i\omega\overline{D} + \overline{J} , \tag{2}$$

$$\nabla \cdot \overline{D} = \rho , \tag{3}$$

$$\nabla \cdot \overline{B} = 0 , \tag{4}$$

where for non bianisotropic media, the constitutive relations [9] can be written as:

$$\overline{D} = \overline{\overline{\varepsilon}} \cdot \overline{E} \quad \text{and} \quad \overline{B} = \overline{\overline{\mu}} \cdot \overline{H} . \tag{5}$$

The permittivity and permeability tensors, in general, will be functions of space. Figure 28 shows the general configuration that we will be using for this section. Using the transformation in [8], the empty sphere of radius c is compressed into a smaller sphere of radius a (region 1), and the empty shell between $r = b$ and $r = c$ is mapped into another shell between $r = a$ and $r = b$ (region 2). Region 3 corresponds to the space where $r > b$. The line at $r = c$ corresponds to the boundary outside which is the region of equivalence. To solve the radiation problem, we need to find the transformed constitutive tensors and solve the transformed problem.
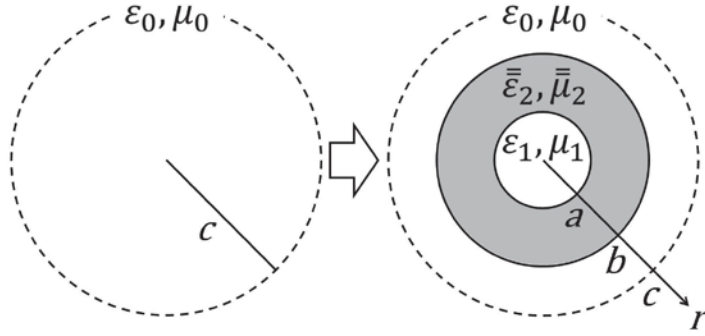
Figure 28 Transformation of Free Space into a Layered Configuration. Left: Original Space. Right: Transformed Space

4.2.2.1   Transformation of the Constitutive Parameters

Since we will eventually be working on the transformed space rather than the original virtual space, in this subsection we will use the unprimed notation to signify the transformed physical space and the primed notation for the virtual space. For other parts of this section, the primed notation is used to represent the source coordinates. Figure 29 shows the relationship between the radius in the physical space r and the radius in the virtual space r'. The region between $r = a$ and $r = b$ has a negative slope, corresponding to space projection. The resulting constitutive parameters are thus expected to have negative real parts. For the r direction,

$$
\begin{aligned}
r' &= \tfrac{c}{a}r & \text{for } r < a\,, \\
r' &= -Ar + B & \text{for } a < r < b,\ \text{and} \\
r' &= r & \text{for } r > b\,.
\end{aligned}
\tag{6}
$$

In region 2,

$$
A = \frac{c-b}{b-a} \quad \text{and} \quad B = \frac{b(c-a)}{b-a}\ .
\tag{7}
$$

Under this transformation, θ and φ are unchanged, thus $\theta = \theta'$ and $\varphi = \varphi'$.
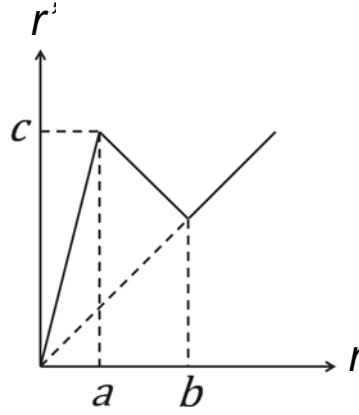
Figure 29 The Relationship Between the Radius in the Physical Space *r* and the Radius in the Virtual Space *r'*

Using the Jacobian [10], the transformed ε and μ can be expressed in terms of the original constitutive tensors:

$$\overline{\overline{\varepsilon}} = \frac{\overline{\overline{J}}_{rr'} \cdot \overline{\overline{\varepsilon}}' \cdot \overline{\overline{J}}_{rr'}^T}{|\overline{\overline{J}}_{rr'}|} \quad \text{and} \quad \overline{\overline{\mu}} = \frac{\overline{\overline{J}}_{rr'} \cdot \overline{\overline{\mu}}' \cdot \overline{\overline{J}}_{rr'}^T}{|\overline{\overline{J}}_{rr'}|} . \tag{8}$$

In spherical coordinates, the Jacobian takes the form:

$$\overline{\overline{J}}_{rr'} = \begin{bmatrix} \dfrac{\partial A_r}{\partial r'} & \dfrac{1}{r'}\dfrac{\partial A_r}{\partial \theta'} & \dfrac{1}{r'\sin\theta'}\dfrac{\partial A_r}{\partial \phi'} \\ \dfrac{r\partial A_\theta}{\partial r'} & \dfrac{r}{r'}\dfrac{\partial A_\theta}{\partial \theta'} & \dfrac{r}{r'\sin\theta'}\dfrac{\partial A_\theta}{\partial \phi'} \\ \dfrac{r\sin\theta\partial A_\phi}{\partial r'} & \dfrac{r\sin\theta}{r'}\dfrac{\partial A_\phi}{\partial \theta'} & \dfrac{r}{r'}\dfrac{\partial A_\phi}{\partial \phi'} \end{bmatrix} . \tag{9}$$

The resulting Jacobian is a constant in region 1 and region 3, and it is diagonal in region 2:

$$\begin{array}{ll} \overline{\overline{J}}_{rr'} = \overline{\overline{I}}\dfrac{a}{c} & \text{for } r < a , \\ \overline{\overline{J}}_{rr'} = \text{diag}[-\tfrac{1}{A}, \tfrac{r}{r'}, \tfrac{r}{r'}] & \text{for } a < r < b, \text{ and} \\ \overline{\overline{J}}_{rr'} = \overline{\overline{I}} & \text{for } r > b . \end{array} \tag{10}$$

Using these results in (10), we have:

$$\begin{array}{ll} \dfrac{\varepsilon_1}{\varepsilon_0} = \dfrac{\mu_1}{\mu_0} = \dfrac{c}{a} & \text{for } r < a , \\ \dfrac{\overline{\overline{\varepsilon}}_2}{\varepsilon_0} = \dfrac{\overline{\overline{\mu}}_2}{\mu_0} = \text{diag}[-\dfrac{(-Ar+B)^2}{Ar^2}, -A, -A] & \text{for } a < r < b, \text{ and} \\ \dfrac{\varepsilon_3}{\varepsilon_0} = \dfrac{\mu_3}{\mu_0} = 1 & \text{for } r > b . \end{array} \tag{11}$$

Note that in the above expression for region 2, *A* and *B* are positive numbers and consequently the constitutive parameters in the physical space for the shell region have negative real parts. This is consistent with the planar case in which space projection results in negative permittivity and permeability. Because we will be analyzing the effects of loss, we introduce a factor of (1

−iδ) to both ε and μ in region 2, where δ is the loss tangent. Note that in region 1 both ε_1 and μ_1 are scalar constants, and in region 2 the transverse components are constant. Only the radial components in region 2 are functions of the radius r.

4.2.2.2 Solution to the Wave Equation

In this subsection we consider a radiator inside a radially inhomogeneous and anisotropic shell as a result of the coordinate transformation presented in the previous section. This problem can be solved analytically by matching the boundary conditions. To facilitate this effort, we will use the formulation based on Mie scattering [9] [10] [11]. Consider the Hertzian dipole shown in Figure 30, oriented in the $\hat{\alpha}$ direction, and positioned at $(r^1, \theta^1, \varphi^1)$ in region 1. Decomposing the waves in all three regions into TM and TE components with respect to $\hat{r}$, we can express the electric and magnetic fields in terms of the Debye potentials π_e and π_m. For TM modes,

$$\overline{H}_{\text{TM}} = \nabla \times \hat{r} \Phi_{\text{TM}} = \nabla \times \overline{r}\pi_e \ , \tag{12}$$

$$\overline{E}_{\text{TM}} = \frac{1}{-i\omega}(\overline{\overline{\varepsilon}}^{-1} \cdot \nabla \times \nabla \times \overline{r}\pi_e) \ . \tag{13}$$

For TE modes,

$$\overline{E}_{\text{TE}} = \nabla \times \hat{r}\Phi_{\text{TE}} = \nabla \times \overline{r}\pi_m \ , \tag{14}$$

$$\overline{H}_{\text{TE}} = \frac{1}{i\omega}(\overline{\overline{\mu}}^{-1} \cdot \nabla \times \nabla \times \overline{r}\pi_m) \ . \tag{15}$$

We can also use the potentials to represent D and B instead of E and H [12] [13].
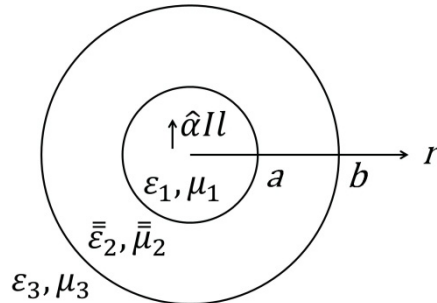
Figure 30 Configuration of the Problem. The Dipole is Oriented Arbitrarily in the $\hat{\alpha}$ Direction in Region 1

Using the Maxwell equations, we can now form the wave equations for π_e and π_m. Here, we will show the procedure for TM modes, noting that the corresponding results for TE modes can be obtained by invoking duality. For TM modes, the wave equation can be written as:

$$\nabla \times \frac{1}{-i\omega}(\overline{\overline{\varepsilon}}^{-1} \cdot \nabla \times \nabla \times \overline{r}\pi_e) = i\omega\overline{\overline{\mu}} \cdot \nabla \times \overline{r}\pi_e . \tag{16}$$

Note that only the transverse components of the permeability tensor will be used, and μ can effectively be treated as μ_t. Also, since ε and μ are not functions of r and are constant, we can expand both sides and equate the arguments of the curl operators with the addition of the gradient of a scalar potential Φ to obtain:

$$\frac{1}{\omega^2} \begin{bmatrix} \frac{1}{\mu_t \varepsilon_r} \frac{1}{r} \frac{1}{r\sin\theta} \left[\frac{\partial}{\partial\theta}\left(-\sin\theta \frac{\partial r\pi_e}{\partial\theta}\right) - \frac{1}{\sin\theta}\frac{\partial^2 r\pi_e}{\partial\phi^2} \right] \\ \frac{1}{\mu_t \varepsilon_t} \frac{1}{r} \frac{\partial}{\partial r}\left(\frac{\partial r\pi_e}{\partial\theta}\right) \\ \frac{1}{\mu_t \varepsilon_t} \frac{1}{r} \frac{1}{\sin\theta} \frac{\partial}{\partial r}\left(\frac{\partial r\pi_e}{\partial\phi}\right) \end{bmatrix} = \begin{bmatrix} r\pi_e + \frac{\partial\Phi_e}{\partial r} \\ \frac{1}{r}\frac{\partial\Phi_e}{\partial\theta} \\ \frac{1}{r\sin\theta}\frac{\partial\Phi_e}{\partial\phi} \end{bmatrix} . \tag{17}$$

For $\hat{\theta}$ and $\hat{\phi}$ components,

$$\frac{1}{\omega^2}\frac{1}{\mu_t\varepsilon_t}\frac{\partial}{\partial\theta}\frac{\partial r\pi_e}{\partial r} = \frac{\partial\Phi_e}{\partial\theta} \quad \text{and} \quad \frac{1}{\omega^2}\frac{1}{\mu_t\varepsilon_t}\frac{\partial}{\partial\phi}\frac{\partial r\pi_e}{\partial r} = \frac{\partial\Phi_e}{\partial\phi} . \tag{18}$$

We can thus obtain Φ_e as:

$$\Phi_e = \frac{1}{\omega^2}\frac{1}{\mu_t\varepsilon_t}\frac{\partial r\pi_e}{\partial r} . \tag{19}$$

Using this result, we have the following for the $\hat{r}$ component:

$$\frac{\varepsilon_r}{\varepsilon_t}\frac{1}{r}\frac{\partial^2 r\pi_e}{\partial r^2} + \frac{1}{r^2\sin\theta}\frac{\partial}{\partial\theta}\left(\sin\theta\frac{\partial\pi_e}{\partial\theta}\right) + \frac{1}{r^2\sin^2\theta}\frac{\partial^2\pi_e}{\partial\phi^2} + k_t^2\frac{\varepsilon_r}{\varepsilon_t}\pi_e = 0 , \tag{20}$$

where k_t is the wavenumber corresponding to the transverse constitutive parameters with respect to r. This is the wave equation for π_e. If we define:

$$\nabla_t^2\pi_e = \nabla^2 - \frac{1}{r^2}\frac{\partial}{\partial r}\left(r^2\frac{\partial\pi_e}{\partial r}\right)$$
$$= \frac{1}{r^2\sin\theta}\left[\frac{\partial}{\partial\theta}\left(\sin\theta\frac{\partial\pi_e}{\partial\theta}\right)\right] + \frac{1}{r^2\sin^2\theta}\frac{\partial^2\pi_e}{\partial\phi^2} , \tag{21}$$

we can simplify the wave equation to:

$$\frac{\varepsilon_r}{\varepsilon_t}\frac{1}{r}\frac{\partial^2 r\pi_e}{\partial r^2} + \nabla_t^2\pi_e + k_t^2\frac{\varepsilon_r}{\varepsilon_t}\pi_e = 0 . \tag{22}$$

In particular, when $\varepsilon_r = \varepsilon_t$ and $\mu_r = \mu_t$,

$$(\nabla^2 + k^2)\pi_e = 0 , \tag{23}$$

and the Helmholtz equation is recovered. This is the case for region 1 and 3.

Approved for public release; distribution is unlimited.

We can now use the separation of variables to solve for π_e. We do so by letting $\pi_e = f_r(r)f_\theta(\theta)f_\varphi(\varphi)$. Regarding f_φ, we have:

$$\frac{d^2 f_\phi}{d\phi^2} + q^2 f_\phi = 0 \text{ and } f_\phi = e^{\pm im\phi} \text{ ,} \tag{24}$$

where m is an integer from 0 to n. For f_θ, we have:

$$\frac{1}{\sin\theta}\frac{d}{d\theta}(\sin\theta \frac{df_\theta}{d\theta}) + (p^2 - \frac{q^2}{\sin^2\theta})f_\theta = 0 \text{ .} \tag{25}$$

In terms of $\cos\theta$, with $p = n(n+1)$, we have:

$$(1-\cos^2\theta)\frac{d^2 f_\theta}{d(\cos\theta)^2} - 2\cos\theta\frac{df_\theta}{d\cos\theta} + \left[n(n+1) - \frac{m^2}{1-\cos^2\theta}\right]f_\theta = 0 \text{ ,} \tag{26}$$

for which the associated Legendre polynomials are solutions to. Thus $f_\theta = P_n^m(\cos\theta)$, where n is an integer from 0 to ∞. Using the results for f_φ and f_θ, regarding f_r we have:

$$\frac{\varepsilon_r}{\varepsilon_t}r\frac{d^2 r f_r}{dr^2} + \left[\frac{\varepsilon_r}{\varepsilon_t}k_t^2 r^2 - n(n+1)\right]f_r = 0 \text{ .} \tag{27}$$

At this point we can put in the explicit r dependence :

$$\frac{\varepsilon_t}{\varepsilon_r} = (\frac{r}{r-R})^2 \text{ ,} \quad \text{in which} \quad R = \frac{b(c-a)}{(c-b)} \text{ .} \tag{28}$$

Rewriting, we have:

$$r\frac{d^2 r f_r}{dr^2} + \left[k_t^2 r^2 - \frac{r^2}{(r-R)^2}n(n+1)\right]f_r = 0 \text{ .} \tag{29}$$

If for f_r we write $f_r(r) = r^{-1}F(k_t \tilde{r})$, where $\tilde{r} = (r - R)$, it is readily shown that F satisfies the Riccati-Bessel equation [14] [15]:

$$(k_t \tilde{r})^2 F'' + [(k_t \tilde{r})^2 - n(n+1)]F = 0 \text{ ,} \tag{30}$$

where $F = \hat{b}_n$ denotes the Riccati-Bessel function, defined as:

$$\hat{b}_n(k_t \tilde{r}) = (k_t \tilde{r})b_n(k_t \tilde{r}) \text{ ,} \tag{31}$$

in which b_n is the spherical Bessel function. In our case, we only use the spherical Bessel function of the first kind (j_n) and the spherical Hankel function of the first kind ($h^{(1)}$). Because we will only use the spherical Hankel function of the first kind, we suppress the superscript and use h_n from here onwards. The general solution for $\pi_{e/m}$ will thus be a double summation over both m and n, where for each m, n:

$$\pi_{e/m} = \frac{1}{r}\hat{b}_n(k_t \tilde{r})P_n^m(\cos\theta)e^{\pm im\phi} \text{ ,} \tag{32}$$

in which $\hat{b}_n(k_t\tilde{r})$ is either $\hat{j}_n(k_t\tilde{r}) = (k_t\tilde{r})j_n(k_t\tilde{r})$ or $\hat{h}_n(k_t\tilde{r}) = (k_t\tilde{r})h_n(k_t\tilde{r})$. When the medium is homogeneous and isotropic, we can simply set $k_t = k$ and $R = 0$. Throughout this section, it is useful to note that:

$$j_n(z) = \sqrt{\frac{\pi}{2z}} J_{n+\frac{1}{2}}(z) , \tag{33}$$

$$h_n(z) = \sqrt{\frac{\pi}{2z}} \left[J_{n+\frac{1}{2}}(z) + iY_{n+\frac{1}{2}}(z) \right] , \tag{34}$$

in which J and Y are the cylindrical Bessel functions of the first and second kind with fractional order n + 1/2. Also, for the derivatives, we have:

$$\hat{b}'_n(z) = (z)b_{n-1}(z) - nb_n(z) , \tag{35}$$

$$\frac{d}{d\theta}P_n^m(\cos\theta) = \frac{1}{\sin\theta} \left[(n\cos\theta)P_n^m(\cos\theta) - (m+n)P_{n-1}^m(\cos\theta) \right] . \tag{36}$$

These expressions are useful for implementing $\hat{b}_n$ and evaluating the fields numerically.

4.2.2.3 Fields and Boundary Conditions

In general, the fields will contain both TM and TE components. We can express the electric and magnetic fields in terms of π_e and π_m. For the radial components:

$$E_r = -\frac{1}{i\omega\varepsilon_t}\left(\frac{\partial^2 r\pi_e}{\partial r^2} + k_t^2 r\pi_e\right) \tag{37}$$

and

$$H_r = \frac{1}{i\omega\mu_t}\left(\frac{\partial^2 r\pi_m}{\partial r^2} + k_t^2 r\pi_m\right) . \tag{38}$$

For the transverse components, using the notation in [11], we have:

$$\begin{bmatrix} E_\theta \\ E_\phi \end{bmatrix} = \begin{bmatrix} \frac{i}{\omega\varepsilon_t}\frac{1}{r}\frac{\partial^2}{\partial r\partial\theta}r & \frac{1}{\sin\theta}\frac{\partial}{\partial\phi} \\ \frac{i}{\omega\varepsilon_t}\frac{1}{r\sin\theta}\frac{\partial^2}{\partial r\partial\phi}r & -\frac{\partial}{\partial\theta} \end{bmatrix} \cdot \begin{bmatrix} \pi_e \\ \pi_m \end{bmatrix} \tag{39}$$

and

$$\begin{bmatrix} H_\theta \\ H_\phi \end{bmatrix} = \begin{bmatrix} \frac{1}{\sin\theta}\frac{\partial}{\partial\phi} & -\frac{i}{\omega\mu_t}\frac{1}{r}\frac{\partial^2}{\partial r\partial\theta}r \\ -\frac{\partial}{\partial\theta} & -\frac{i}{\omega\mu_t}\frac{1}{r\sin\theta}\frac{\partial^2}{\partial r\partial\phi}r \end{bmatrix} \cdot \begin{bmatrix} \pi_e \\ \pi_m \end{bmatrix} . \tag{40}$$

These expressions can be used for all three regions to find the fields and match the boundary conditions.

The boundary conditions consist of matching the fields at the source and the interfaces. For the source, which in our case exists only in region 1, we use the expansion of a Hertzian dipole. Consider a dipole moment. For the TM components, we have:

$$\pi_e^i = \frac{i}{4\pi} \frac{I\ell}{k_1} \hat{\alpha} \cdot \nabla' \times \nabla' \times \hat{r}' \sum_{n=0}^{\infty} \sum_{m=-n}^{n} \frac{(2n+1)(n-|m|)!}{n(n+1)(n+|m|)!}$$

$$\frac{1}{r}\hat{j}_n(kr_<)\hat{h}_n(kr_>)P_n^{|m|}(\cos\theta')P_n^{|m|}(\cos\theta)e^{im(\phi-\phi')} .$$

(41)

For the TE components, we have:

$$\pi_m^i = i\omega\mu_1 \frac{i}{4\pi} \frac{I\ell}{k_1} \hat{\alpha} \cdot \nabla' \times \hat{r}' \sum_{n=0}^{\infty} \sum_{m=-n}^{n} \frac{(2n+1)(n-|m|)!}{n(n+1)(n+|m|)!}$$

$$\frac{1}{r}\hat{j}_n(kr_<)\hat{h}_n(kr_>)P_n^{|m|}(\cos\theta')P_n^{|m|}(\cos\theta)e^{im(\phi-\phi')} .$$

(42)

In these two expressions r', θ', and φ' correspond to the coordinates of the source and the operators $\nabla' \times \nabla' \times$ and $\nabla' \times$ operate only on the source coordinates. Also, $r_< = \min\{r_1, r\}$ and $r_> = \max\{r_1, r\}$, depending on the radius r of the observation point. We note that the factor P is common for each m and n. Upon suppressing, we can simplify the notation for the potentials corresponding to the incident spectrum of waves in region 1 as:

$$\pi_{1<}^i = b_1\hat{j}_n(k_1r) \quad \text{for } r < r' , \text{ and}$$

(43)

$$\pi_{1>}^i = a_1\hat{h}_n(k_1r) \quad \text{for } r > r' .$$

(44)

Furthermore, the forms for π^{TM} and π^{TE} are identical, therefore we can simply use $\pi_{1,2,3}$ for each region, keeping in mind that each $\pi_{1,2,3}$ represents two cases. Thus for region 1, taking into account the reflections at the boundaries [11], we write:

$$\pi_{1<} = a_1\tilde{R}_{12}\hat{j}_n(k_1r) + b_1\hat{j}_n(k_1r) \quad \text{for } r < r' ,$$

(45)

$$\pi_{1>} = a_1[\hat{h}_n(k_1r) + \tilde{R}_{12}\hat{j}_n(k_1r)] \quad \text{for } r > r' .$$

(46)

In region 2, we have:

$$\pi_2 = a_2[\hat{h}_n(k_{2t}\tilde{r}) + R_{23}\hat{j}_n(k_{2t}\tilde{r})] ,$$

(47)

and in region 3,

$$\pi_3 = \tilde{T}_{13}a_1\hat{h}_n(k_3r) .$$

(48)

In the above expressions involving $\pi_{1,2,3}$,

$$a_2 = \frac{T_{12}}{1 - R_{21}R_{23}}a_1 ,$$

(49)

$$\tilde{R}_{12} = R_{12} + \frac{T_{21}R_{23}T_{12}}{1 - R_{21}R_{23}} ,$$

(50)

and

$$\tilde{T}_{13} = \frac{T_{12}T_{23}}{1 - R_{21}R_{23}} . \tag{51}$$

$\tilde{R}_{12}$ and $\tilde{T}_{13}$ are the total reflection and transmission coefficients, which account for the multiple reflections. The reflection and transmission coefficients for each interface can be found by matching the boundary conditions. For example:

$$R_{12}^{\mathrm{TM}} = \frac{\sqrt{\varepsilon_{2t}\mu_{1t}}\hat{h}_n(k_{2t}\tilde{a})\hat{h}'_n(k_{1t}a) - \sqrt{\varepsilon_{1t}\mu_{2t}}\hat{h}'_n(k_{2t}\tilde{a})\hat{h}_n(k_{1t}a)}{\sqrt{\varepsilon_{1t}\mu_{2t}}\hat{j}_n(k_{1t}a)\hat{h}'_n(k_{2t}\tilde{a}) - \sqrt{\varepsilon_{2t}\mu_{1t}}\hat{h}_n(k_{2t}\tilde{a})\hat{j}'_n(k_{1t}a)} , \tag{52}$$

$$R_{21}^{\mathrm{TM}} = \frac{\sqrt{\varepsilon_{2t}\mu_{1t}}\hat{j}_n(k_{2t}\tilde{a})\hat{j}'_n(k_{1t}a) - \sqrt{\varepsilon_{1t}\mu_{2t}}\hat{j}_n(k_{1t}a)\hat{j}'_n(k_{2t}\tilde{a})}{\sqrt{\varepsilon_{1t}\mu_{2t}}\hat{j}_n(k_{1t}a)\hat{h}'_n(k_{2t}\tilde{a}) - \sqrt{\varepsilon_{2t}\mu_{1t}}\hat{h}_n(k_{2t}\tilde{a})\hat{j}'_n(k_{1t}a)} , \tag{53}$$

$$T_{12}^{\mathrm{TM}} = \frac{i\varepsilon_{2t}\sqrt{\mu_{2t}/\varepsilon_{1t}}}{\sqrt{\varepsilon_{1t}\mu_{2t}}\hat{j}_n(k_{1t}a)\hat{h}'_n(k_{2t}\tilde{a}) - \sqrt{\varepsilon_{2t}\mu_{1t}}\hat{h}_n(k_{2t}\tilde{a})\hat{j}'_n(k_{1t}a)} , \tag{54}$$

and

$$T_{21}^{\mathrm{TM}} = \frac{i\varepsilon_{1t}\sqrt{\mu_{1t}/\varepsilon_{2t}}}{\sqrt{\varepsilon_{1t}\mu_{2t}}\hat{j}_n(k_{1t}a)\hat{h}'_n(k_{2t}\tilde{a}) - \sqrt{\varepsilon_{2t}\mu_1}\hat{h}_n(k_{2t}\tilde{a})\hat{j}'_n(k_{1t}a)} . \tag{55}$$

We will also need the coefficients R_{23} and T_{23}, which we can obtain by simply changing subscripts 1 and 2 of R_{12} and T_{12} to 2 and 3, respectively. To obtain the coefficients for TE modes, we can invoke duality by swapping ε and μ.

We now derive the dipole expansion coefficients for a dipole corresponding to each m, n. Evaluating the coefficients for TM and TE modes yield:

$$\begin{aligned} a_1^{\mathrm{TM}} = b_1^{\mathrm{TM}} &= A_{mn}(-\hat{\theta}) \cdot \nabla' \times \nabla' \times \hat{r}'\hat{b}_n(k_1r')P_n^{|m|}(\cos\theta')e^{-im\phi'} \\ &= -A_{mn}\frac{k_1}{r'}\frac{n\cos\theta'}{\sin\theta'}\hat{b}'_n(k_1r')P_n^{|m|}(\cos\theta')e^{-im\phi'} \\ &\quad + A_{mn}\frac{k_1}{r'}\frac{(m+n)}{\sin\theta'}\hat{b}'_n(k_1r')P_{n-1}^{|m|}(\cos\theta')e^{-im\phi'} , \end{aligned} \tag{56}$$

and

$$\begin{aligned} a_1^{\mathrm{TE}} = b_1^{\mathrm{TE}} &= i\omega\mu_1 A_{mn}(-\hat{\theta}) \cdot \nabla' \times \hat{r}'\hat{b}_n(k_1r')P_n^{|m|}(\cos\theta')e^{-im\phi'} \\ &= i\omega\mu_1 A_{mn}\frac{im}{r'\sin\theta'}\hat{b}_n(k_1r')P_n^{|m|}(\cos\theta')e^{-im\phi'} , \end{aligned} \tag{57}$$

where

$$A_{mn} = \frac{i}{4\pi} \frac{I\ell}{k_1} \frac{(2n+1)(n-|m|)!}{n(n+1)(n+|m|)!} . \tag{58}$$

We have now completely formulated the problem for the potentials and fields. In the next section, we will apply this formulation to several different cases.

4.2.3 Results and Discussions

In this section, we will show the computed results based on the formulation de- scribed in the previous section. Subsequently, these computations are used to illustrate various aspects regarding the effects of enhanced virtual apertures. In particular, we are interested in the effects of loss on resolution in the farfield. We will primarily be studying the $\hat{\theta}$-directed electric field in the xy plane. The other field components at other observation points can be obtained in a similar fashion. In the xy plane, $\theta = \pi/2$. For each m and n, the electric field in the $\hat{\theta}$ direction is:

$$E_\theta = a^{\mathrm{TM}} \frac{i}{\omega \varepsilon_t} \frac{k_t}{r} [-(m+n)] \, \hat{b}'_n(k_t\tilde{r}) \mathrm{P}^{|m|}_{n-1}(\cos\theta) e^{im\phi}$$

$$+ a^{\mathrm{TE}} \frac{im}{r} \, \hat{b}'_n(k_t\tilde{r}) \mathrm{P}^{|m|}_n(\cos\theta) e^{im\phi} . \tag{59}$$

In comparison, the corresponding exact expression for the $\hat{\theta}$-directed electric field in the xy plane due to a $\hat{z}$-oriented dipole at the origin in free space is [9]:

$$E_\theta = -i\omega\mu_0 I\ell \frac{e^{ikr}}{4\pi r} \left[1 + \frac{i}{kr} + (\frac{i}{kr})^2 \right] . \tag{60}$$

Then, based on (60), we can calculate the reference value of the expected electric field corresponding to the lossless case.

4.2.3.1 4-Dipole Array in Free Space

We first consider the configuration as shown in Figure 31. In the corresponding virtual space, there is a 4-dipole array in free space. The dipoles are oriented in the $\hat{z}$ direction, and each has an in-phase dipole moment. The dipoles are separated from each other by $\lambda/2$ and are arranged along the x axis. In the transformed space, with $a = 0.25\lambda$, $b = 0.5\lambda$, and $c = 1\lambda$, the effective physical aperture is reduced from c to b, or by a factor of 2. The compression ratio a/c is 0.25. In the ideal case with no loss, we expect the two cases to produce identical fields for $r > c$.
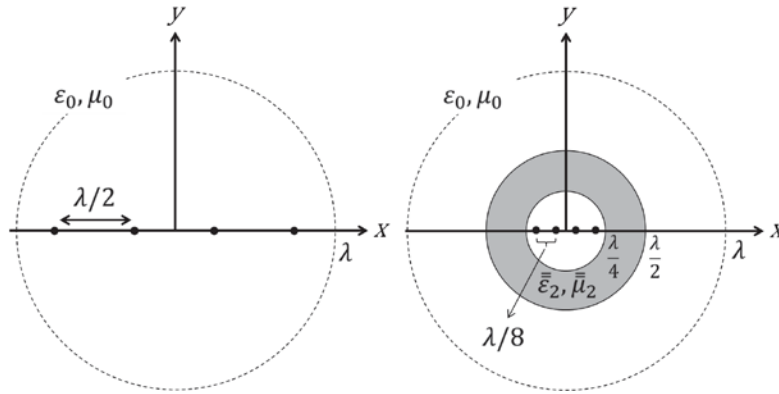
Figure 31 A 4-Dipole Array in Free Space with λ/2 Spacing. In the Transformed Space, *a* = 0.25λ, b = 0.5λ, and c = 1λ. In the Lossless Case, the Regions for r > c are Equivalent

For numerical stability, we use the value of $\delta = 10^{-15}$ to represent the lossless case. In Figure 32 we show the field value $|Re\{E_z\}|$ in the xy plane. The range is between $\pm 6\lambda$ for both axes. The main beams at $\varphi = \pm\pi/2$ as well as the sidelobes are clearly observed. In Figure 33, we show the field value $|Re\{E_z\}|$ in the xy plane for $r > b$. Visually, they look similar in both cases, but, as shown in Figure 34, the fields are in fact different for $b < r < c$. Because of the extremely low-loss and the well-matched condition created by the transformation, high field values not unlike that of surface resonances are observed at points near $r = b$. The field value for $r > c$ converges to the reference value rapidly, as shown in Figure 35.
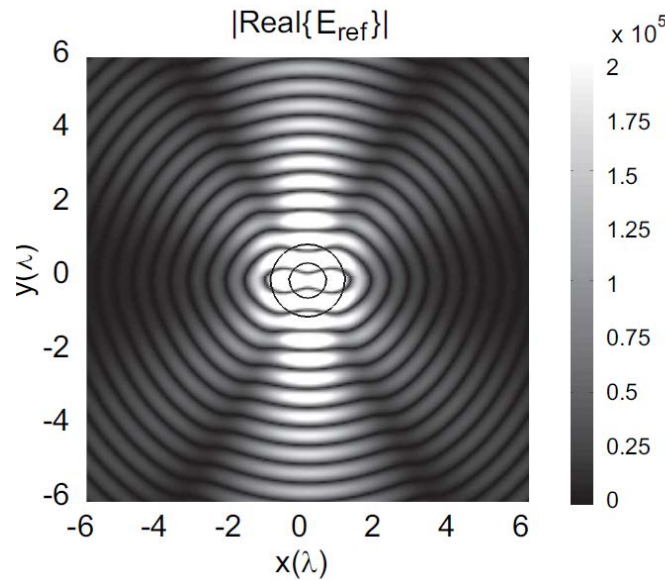
Figure 32 2D Scan of $|Re\{E_z\}|$ in the *XY* Plane Using the Exact Expression. The Inner Circle Corresponds to $r = 0.5\lambda$ and the Outer Circle Corresponds to $r = 1\lambda$
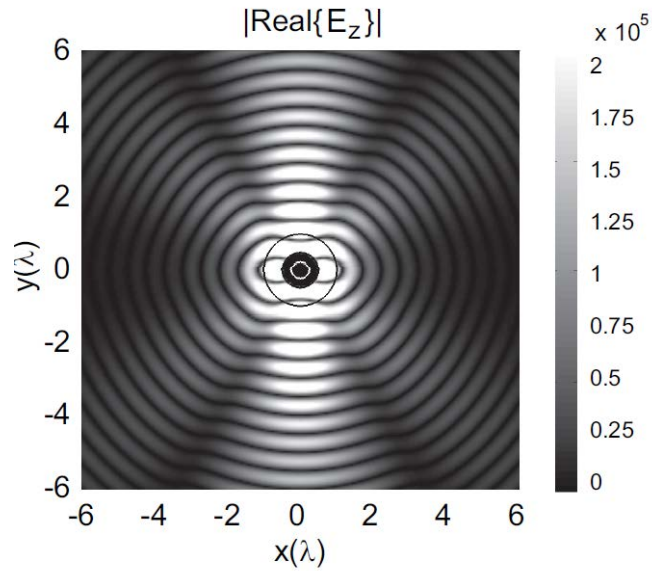
Figure 33 2D Scan of |Re{Ez}| in the XY Plane in Region 3 (r > b) Using the Transformation Method. The Circles Correspond to r = 0.25λ, 0.5λ, and 1λ
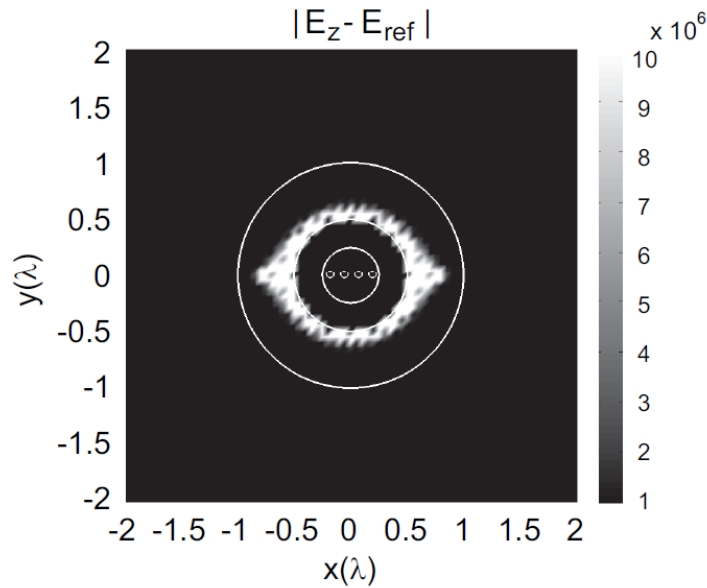
Figure 34 Zoomed 2D Scan of the Magnitude of the Difference Between the Two Methods. The field Values for r > c are Practically Identical While the Field Values for b < r < c are Different. This is Expected Because the Regions of Equivalence are for r > c only
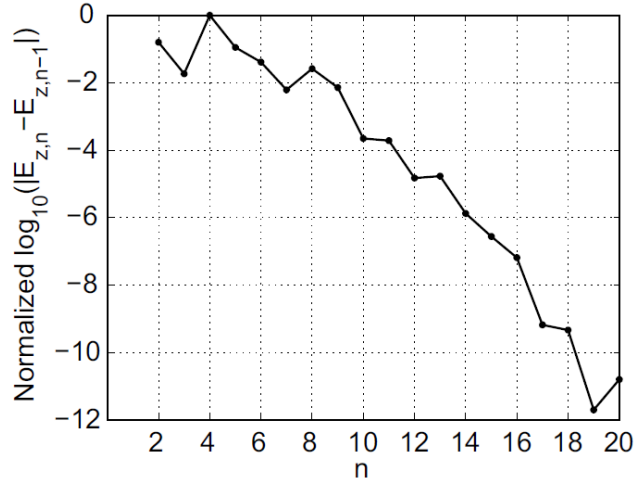
Figure 35 Convergence of the Electric Field Value as *n* Increases

In Figure 36, we plot the magnitude of the electric field component E_θ at r = 100λ, corresponding to the farfield value. The pattern is effectively identical to the reference one. This can also be seen from Figure 37, where we plot the magnitude of the coefficient T_{TM} as a function of n. This is the value of T_{13} shown in section 2 for TM modes given n. The coefficients T_{TE} have the same values as T_{TM} due to the symmetry between ε_2 and μ_2. In the lossless case, $T_{TM} = 0.25$, and it remains the same for all n, suggesting that there is no loss of angular resolution, and the original radiation pattern is preserved. Thus, a physical aperture with diameter λ has formed a virtual aperture with diameter 2λ .
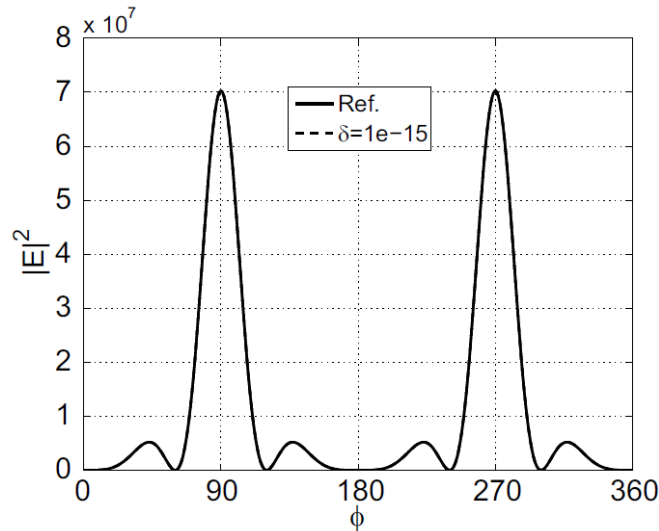
Figure 36 Farfield Radiation Pattern of E_θ for the Physical and Virtual 4-Dipole Array. The Patterns are Essentially Identical Due to the Low Loss Tangent of $\delta = 10{-}15$
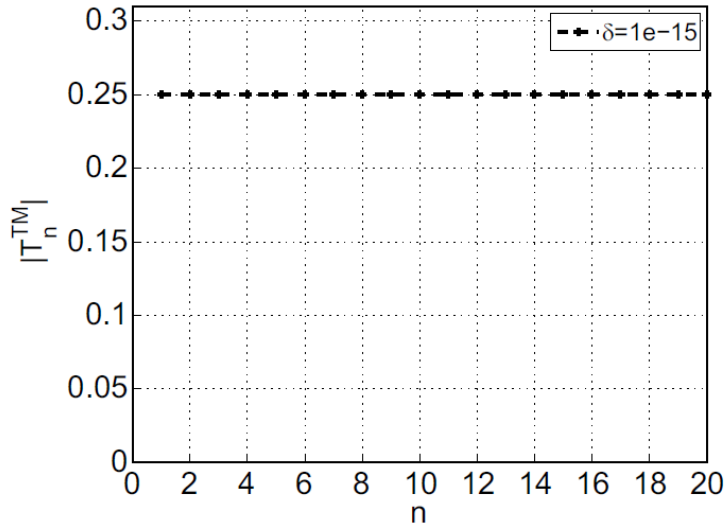
Figure 37 Magnitude of the Coefficient T as a Function of n. The Magnitude is the Same as the Compression Ratio a/c = 0.25 for n from 1 to 20

4.2.3.2 4-Dipole Array with Ground Plane

Consider the configuration as shown in Figure 38. It is similar to the one in Figure 31, except that here the dipole elements are placed $\lambda/4$ above a PEC ground plane. In the transformed space, $a = 0.25\lambda$, $b = 0.5\lambda$, and $c = 1\lambda$. The compression ratio is maintained to be 0.25. Image theory is used here to calculate the fields where we put four dipoles with amplitudes $Il = -1$ at $y = -0.0625\lambda$ so that they form mirror images of the physical dipoles. The region of interest ranges only from $\varphi = 0$ to $\pi/2$, and the maximum electric field strength is expected to be double that of the freespace case. In Figure 39 we plot the farfield radiation pattern of E_θ in the xy plane. The radiation pattern from the virtual antenna formed by a smaller core-shell structure is equivalent to that from a physical antenna with a larger dimension. The mainlobe amplitude and the sidelobe positions agree with the reference case.

Since c can be arbitrarily large, it would seem that we can theoretically use this method to build a structure with a smaller dimension and achieve an aperture with arbitrarily large directivity. However, there are several effects we need to consider, including coupling and loss. By virtue of the equivalence due to the transformation, dipole coupling is no worse than the situation in the virtual space, despite the spacing between the elements being physically much closer. However, loss will introduce substantial modifications to the radiated power and beamwidth. This effect is shown in the same figure, in which increasing the loss causes a reduction in directivity and an expanded beamwidth. The magnitude of the beam also decreases significantly as the loss tangent goes up. The loss also introduces both mismatches as well as ohmic loss into the system.

In Figure 40, we plot the magnitude of the coefficient T^{TM} as a function of n for different loss values. It is observed that for a low loss tangent of $\delta = 10^{-4}$, the transmission coefficients remain the same as before up to n = 12. As the loss increases, $|T\ TM|$ decreases more rapidly. For example, when $\delta = 10^{-2}$, the rolloff occurs at n = 6, contributing to the decrease of farfield resolution.

In Figure 41, we plot the farfield radiation pattern of E_θ in the xy plane for $c = 2\lambda$ instead of 1λ. Hence, the compression ratio changes from 0.25 to 0.125. The decay of performance is now even more rapid than in the previous case. For the same δ as before, we now have degraded beamwidth and magnitude. This is also evident from the plot of the transmission coefficients in Figure 42, where the rolloff occurs for smaller n.

Figure 38 A 4-Dipole Array with $\lambda/2$ Element Spacing Positioned $\lambda/4$ above a PEC Ground Plane. In the Transformed Space, $a = 0.25\lambda$, $b = 0.5\lambda$, and $c = 1\lambda$. Image Theory is Used to Calculate the Fields

Figure 39 Farfield Radiation Pattern of E_θ Corresponding to Various δ for the Physical and Virtual 4-Dipole Array Positioned Over a Ground Plane. The Compression Ratio is 0.25 in this Case
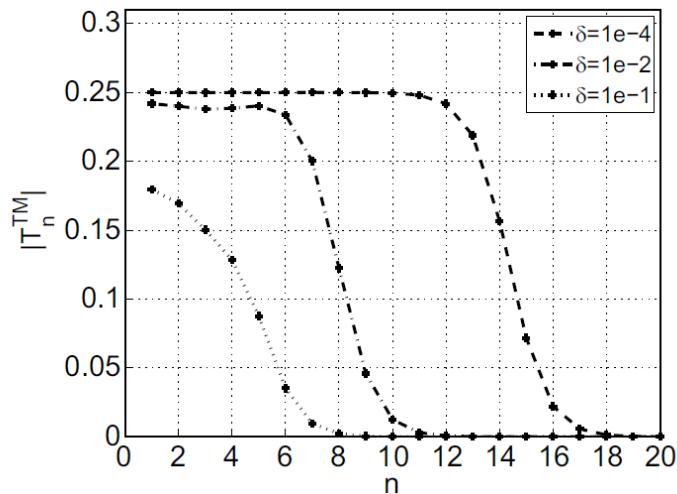
Figure 40 Magnitude of the Coefficient T^{TM} as a Function of n. The Magnitude Decreases as n Increases. The Decay is Faster for a Higher Loss Value
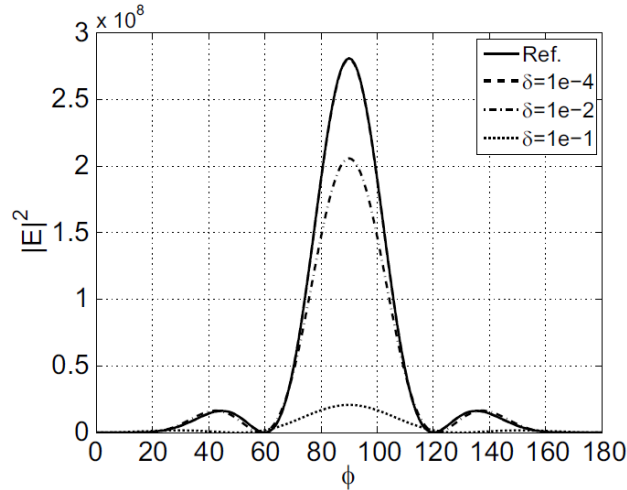
Figure 41 Farfield Radiation Pattern of E_θ Corresponding to Various δ for the Physical and Virtual 4-Dipole Array Positioned Over a Ground Plane. The Compression Ratio is 0.125 in this Case
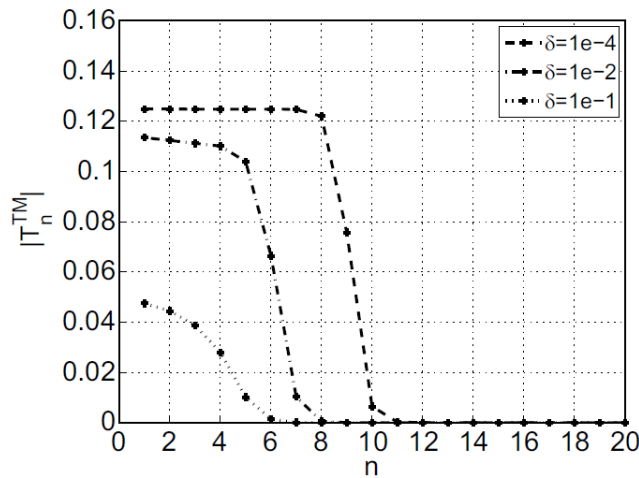
Figure 42 Magnitude of the Coefficient T_n^{TM} as a Function of n. The Magnitude Decreases as n Increases. The Decay is Further Increased Due to the Higher Compression

4.2.3.3 8-Dipole Array with Ground Plane

Maintaining the same compression ratio of $a/c = 0.125$ and element spacing in the virtual space as in the 4-dipole configuration, we now change the number of dipoles to 8, keeping the same spacing in the virtual space. In Figure 43, the gray dots indicate the dipole positions in the virtual space and the black dots correspond to the transformed ones. When we had 4 dipoles for the same compression ratio, we were not taking advantage of the gain in virtual aperture size. Here, we are now taking advantage of the virtual aperture size with a gain factor of 4, from a physical aperture of 1λ to a virtual aperture of 4λ. In Figure 44, it is seen that when we have δ = 10^{-4}, the performance is discernibly different from the reference case. We observe a more dramatic change in the radiation patterns for each corresponding increase in δ. The same trend for $|T^{TM}|$ is illustrated in Figure 45.
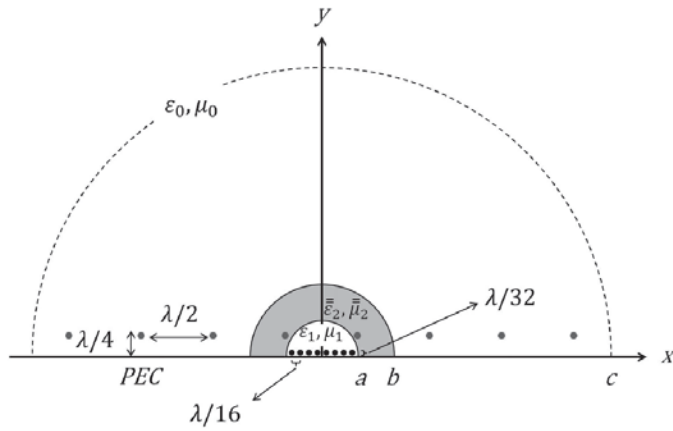
Figure 43 An 8-Dipole Array Positioned λ/4 Above a PEC Ground Plane with λ/2 Element Spacing. In the Transformed Space, $a = 0.25\lambda$, $b = 0.5\lambda$, and $c = 2\lambda$. Image Theory is Used to Calculate the Fields
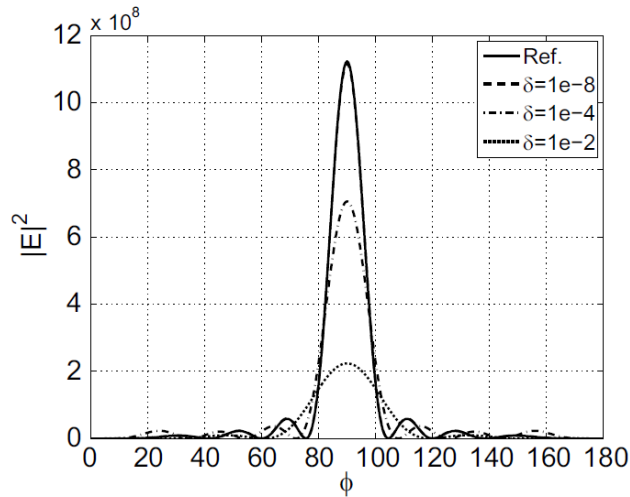
Figure 44 Farfield Radiation Pattern of E_θ Corresponding to Various δ for the Physical and Virtual 8-Dipole Array Positioned Over a Ground Plane. The Compression Ratio is 0.125 in This Case
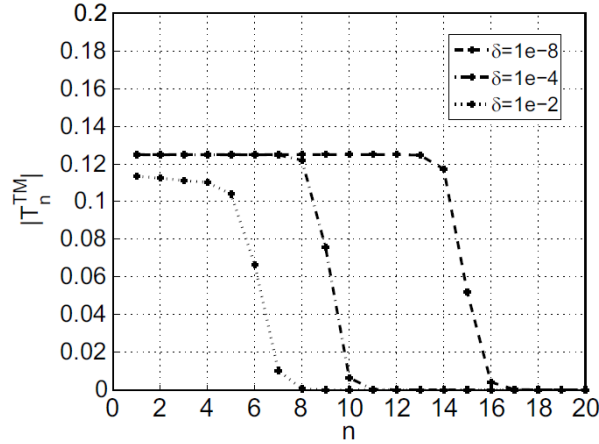
Figure 45 Magnitude of the Coefficient T^{TM} as a Function of n. The Magnitude Decreases as n Increases. The Decay Follows the Same Trend as Before

4.2.3.4   Virtual Aperture and Farfield Resolution

Clearly, there is a relationship between the transmission coefficients, the beamwidth, and the loss tangent δ. In this subsection, we will investigate this issue. For each previous case where the compression ratio is 0.125, we can numerically solve for the null-to-null beamwidth of E_θ by starting from the normal direction ŷ and scanning for a φ that corresponds to the first minimum field value. The results are shown in Figure 46 and Figure 47. The horizontal axes correspond to the loss tangent in a log10 scale and the vertical axis is the null-to-null beamwidth in degrees. In Figure 46, for the 4-dipole case subject to a loss tangent smaller than 10^{-3}, the beamwidth converges to 60°, corresponding to the lossless case. It gradually diverges to approximately 80° as the loss tangent reaches 10^{-1}. In Figure 47, for the 8-dipole case, even when the loss tangent is 10^{-5}, the beamwidth does not converge to the value of the lossless case. It also gradually diverges to approximately 80° as the loss tangent approaches 10^{-1}. However, here the overall angle deviation is larger. For the same range in δ, the angle now changes by 50° rather than 20°. Even though the traces of the plots are not linear with respect to $\log_{10} \delta$, the expansion of the beam clearly relates more closely to the log of δ rather than just δ itself.

In addition to observing the changes in beamwidth, we can also look at how the coefficients T change with n. T are the TM/TE transmission coefficients from region 1 to region 3 for each n. Their complex values are different for each n in the presence of loss. In Figure 48 and Figure 49, we show the 3D plots of T as a function of n and δ , where a = 0.25λ , b = 0.5λ , and c = 1λ or 2λ. The three axes correspond to n, log10 δ, and T. When the compression ratio is 0.25, T = a/c = 0.25 for the lossless case, and it is 0.125 for a/c = 0.125.

In the first plot (Figure 48), with a compression ratio of 0.25, the flat region of T is rather large and a cliff-like structure is observed. The edge starts approximately from n = 8 on the n axis to log10 δ = −5 on the δ axis. In the second plot (Figure 49), with a compression ratio of 0.125, the flat region of T is smaller and a cliff-like structure is observed again. The edge starts approximately from n = 8 on the n axis to log10 δ = −10 on the δ axis. These two plots show quantitatively how the transmission coefficients vary with n and δ.

For comparison, consider a sphere with characteristic dimension kr, where k is the wavenumber and r is the radius of the sphere. The maximum number of modes supported is related to kr. Take Figure 50 for example, where we are plotting the same parameters as in Figure 48, except that we use an isotropic medium for region 2, with $\varepsilon_2 = \varepsilon_0 (1 + i\delta)$, and $\mu_2 = \mu_0(1 + i\delta)$. Effectively, the sphere has a radius of a = 0.25λ despite the shell. We keep the medium in region 1 to be the same as the previous case with a/c = 0.25; thus, $k_1 a = 2\pi$. It is seen that T drops extremely fast with respect to n. When the loss tangent is high, we still see a significant drop in amplitude, but we no longer see a diagonal cliff-like shape. This is one reason why by simply putting a radiating source inside a sphere with high dielectric medium alone will not support high angular resolution beyond a certain level regulated by the cutoffs of the transmission coefficients.
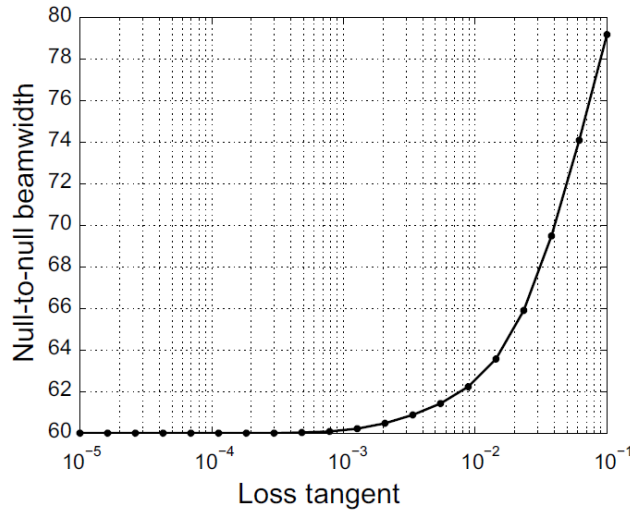
Figure 46 Null-to-null Beamwidth for a 4-Dipole Array with $a = 0.25\lambda$, $b = 0.5\lambda$, and $c = 2\lambda$. A Smooth Transition is Observed as δ Varies
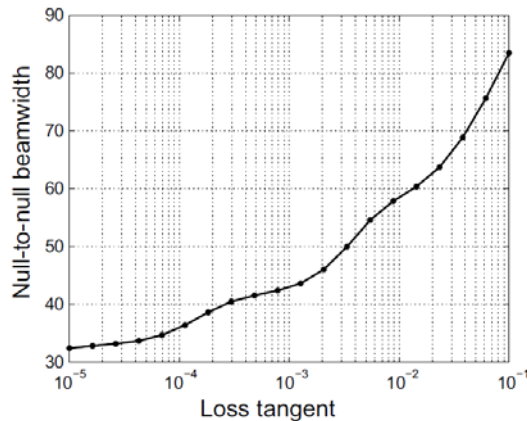
Figure 47 Null-to-null Beamwidth for a 8-Dipole Array with $a = 0.25\lambda$, $b = 0.5\lambda$, and $c = 2\lambda$. The Beamwidth Broadens Faster than the 4-Dipole Case
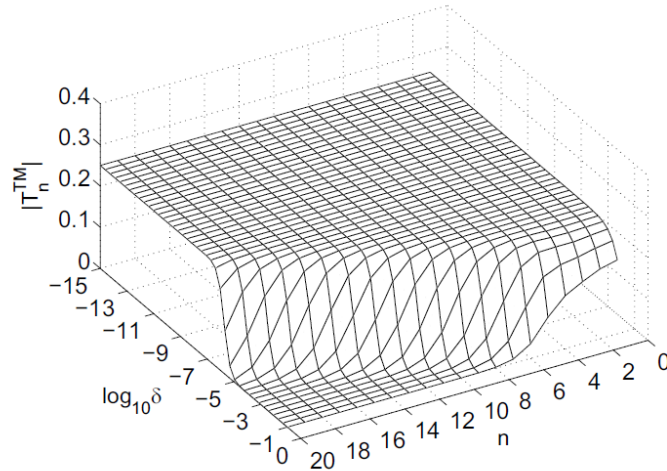
Figure 48 3D Plot of T as a Function of n and δ. a = 0.25λ, b = 0.5λ, and c = 1λ
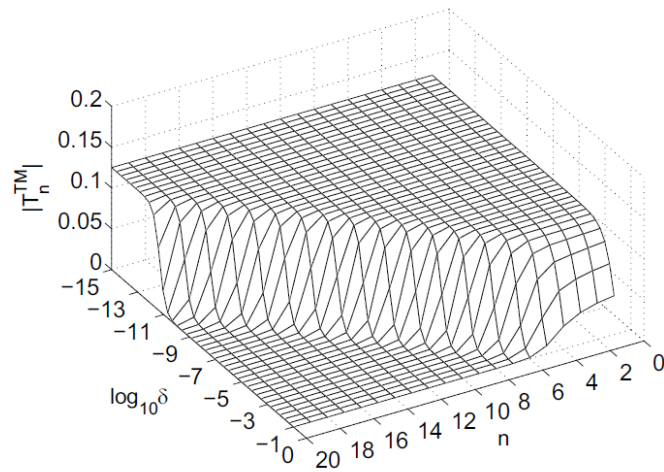
Figure 49 3D Plot of T as a Function of n and δ. a = 0.25λ, b = 0.5λ, and c = 2λ
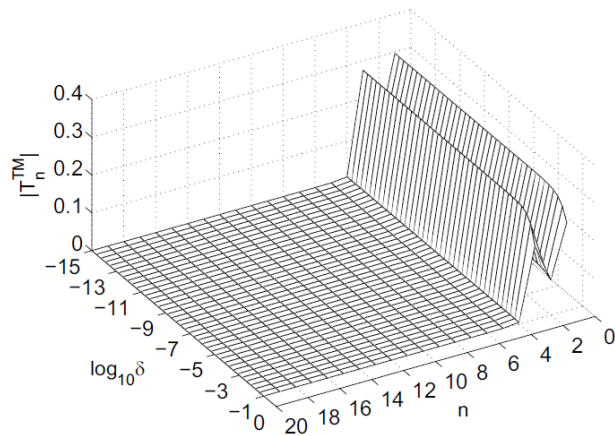
Figure 50 3D Plot of T as a Function of n and δ. a = 0.25λ, b = 0.5λ. Instead of a Transformed Shell, a Regular Shell from r = a to b is used with ε2 = ε0 (1 + iδ) and μ2 = μ0(1 + iδ)

47

Besides studying the effects of the transmission coefficients numerically, we can also look at it analytically. Recall that for each *n*, the transmission coefficient $\tilde{T}_{13}$ can be written as:

$$\tilde{T}_{13} = \frac{T_{12}T_{23}}{1 - R_{21}R_{23}} \quad . \tag{61}$$

In the above equation, T_{12}, T_{23}, R_{21}, and R_{23} themselves are functions of the constitutive and geometrical parameters. Note each one contains the Riccati-Bessel functions and their derivatives. We can look at the arguments of the Riccati-Bessel functions involved, and it is straightforward to show that $k_1 a = k_0 c$. Also, $k_3 b = k_0 b$. Other than the arguments of the Riccati-Bessel functions, the factors $\varepsilon_{2t}\mu_1$ and $\varepsilon_3\mu_2$ are the same as $\varepsilon_1\mu_{2t}$ and $\varepsilon_{2t}\mu_3$, respectively. Therefore, $R_{21} = R_{23} = 0$ and $T_{12}T_{23} = a/c$ for the lossless case.

Because the arguments within each denominator of the single layer coefficients are the same for the lossless case, when loss is present the denominators of R_{21}, R_{23}, T_{12}, T_{23} all perturb around their lossless Wronskian value of "i". Whereas the nominators of T_{12} and T_{23} remain close to a/c under perturbation, the nominators of R_{21} and R_{23} are extremely sensitive to δ. Based on this, it can be shown that within the scope of this chapter, the contour of the following equation yields a rough estimate on the cutoffs of the transmission coefficients:

$$\left| \left(\hat{j}_n(R_1')\hat{j}_n'(R_1) - \hat{j}_n(R_1)\hat{j}_n'(R_1') \right) \left(\hat{h}_n(R_2')\hat{h}_n'(R_2) - \hat{h}_n(R_2)\hat{h}_n'(R_2') \right) \right| = 1 \; , \tag{62}$$

It should be noted that for planar slabs with the real parts of the constitutive parameters as $(-\varepsilon_0, -\mu_0)$ and similar loss tangent relationships as in the cases shown here, the spatial resolution in terms of the maximum tangential wavenumber before transmission cutoff is governed by a simple expression: $(1/d) \ln(2/\delta)$, where δ is the loss tangent and d is the thickness of the slab. In both the planar and spherical cases, the rapid deterioration of the spatial and angular resolution is related to the log of δ. The difference is that in the virtual aperture case considered here, the geometry is spherical and the angular harmonics are discrete rather than continuous like the tangential wavenumber of a slab. Consequently, one cannot directly solve for the resolution. However, one can plot the corresponding contour via interpolation. The contour plots for the two virtual aperture cases discussed in this subsection are shown in Figure 51 and Figure 52. The contours correspond to the edges of the cliff-like shapes in the previous 3D plots. It is seen that the contours provide reasonable estimates for the cutoffs of the transmission coefficients and hence the farfield resolution.
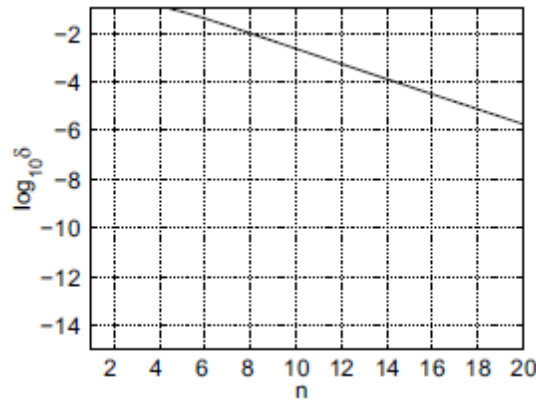
Figure 51 Interpolated Contour Plot as a Function of *n* and δ. $c = 1\lambda$. The Upper Right Region C orresponds to the Cutoffs of the Transmission Coefficients and Loss of Resolution
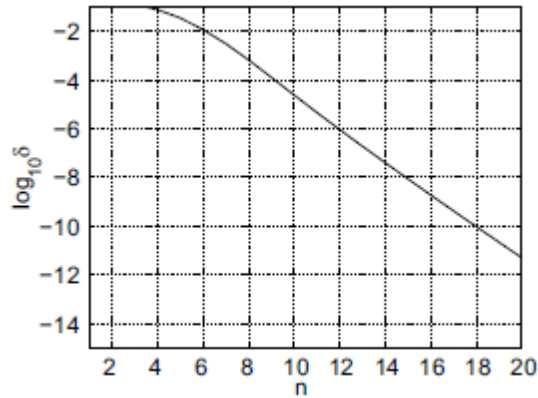
Figure 52 Interpolated Contour Plot as a Function of *n* and δ. $c = 2\lambda$. The Upper Right Region Corresponds to the Cutoffs of the Transmission Coefficients and Loss of Resolution

4.2.4 Conclusion

In this chapter, we proposed a spherical core-shell structure which can achieve arbitrarily large directivity. The structure was predicted and obtained from the proper coordinate transformations. A large virtual aperture can be projected to free space with a small physical dimension, subsequently leading to a large directivity. We investigated the problem by finding the transformed constitutive tensors and solving the equivalent problem in the core-shell configuration. Using the Ricatti-Bessel functions, we can represent the field components with Debye potentials and subsequently solve for the fields in all regions. We applied the formulation to several cases of dipole arrays within the shell, corresponding to both free-space and half-space problems in the virtual space. Both the near field and farfield phenomena were investigated. The relationship between the beamwidths and transmission coefficients for different loss values has been studied and an estimation for the cutoffs of the transmission coefficients was provided. Overall, the loss is linked directly to the farfield resolution in terms of the available angular harmonics. It is found that the deterioration of beamwidth changes rapidly with the increase of loss tangent in the shell medium. Even though one can theoretically construct an antenna aperture with arbitrarily high directivity in a small package, based on the specific transformation used here, there is a practical limit as to how strongly a large aperture can be com- pressed into a small one. It can be reasoned that if a moderate loss tangent value can be reached, a virtual aperture gain factor of at least two should be achievable.

5 Subtask 4: An Electric and Magnetic Dipole Antenna for Zero Backscatter and Low Radiation Quality Factor

The original goal of the effort was to establish performance limits for antennas mounted on structures (e.g. UAS, Micro-UAS, etc.) with sub-wavelength dimensions. However, this goal was revised because other researchers achieved a significant portion of the proposed research. The new goal of this effort is to use analytical and numerical methods to examine the possibility of using a Huygens source (crossed electric and magnetic dipole) to achieve a low Q and/or a low backscatter antenna.

5.1 Objectives

The objective is to use analytical and numerical methods to examine the possibility of using a Huygens source to realize an antenna the can approach the Wheeler-Chu Q Limit and to realize a low or zero backscatter antenna. While the main emphasis has been achieving a low backscatter antenna which can be used as a near field probe, there are a number of applications for controlling absorption and scattering processes from antennas. For example, a Huygens source can also be used to realize a thin layer perfect absorbing material. By utilizing antenna scattering principles, it is possible to design absorbing materials at high frequencies where magnetic materials are not possible [16,17]. We can also use antenna scattering principles in the design of wireless power transfer (WPT) systems. For this application, antenna scattering can be used to increase power transfer which is important consideration in wireless charging and near-field communication (NFC) devices [18].

5.2 Technical Summary

Before we begin to discuss the design and realization of a zero backscatter Huygens source we must provide an overview of antenna scattering in general. In the following sections this is accomplished by first introducing the generalized scattering matrix and discussing the different ways to decompose the scattered field of an antenna. We then proceed to discuss the basic approaches for controlling scattering and the important role that absorbed power plays in controlling scattering. After concluding the overview of antenna scattering we then proceed to discuss scattering from an ideal Huygens source. This is followed by a discussion of the realization of the Huygens source and several implementation issues.

5.2.1 Generalized Scattering Matrix

The generalized scattering matrix, S, relates the outgoing portion of the total field to the incoming portion of the total field by the following equation

$$\begin{pmatrix} Outgoing \\ Modes \end{pmatrix} = S \begin{pmatrix} Incoming \\ Modes \end{pmatrix} \tag{63}$$

The scattered field can be found in terms of a S-matrix by noting that when no scatter is present the scattering matrix reduces to the identity matrix I. In this case, the incoming and

Approved for public release; distribution is unlimited.

outgoing modes combine to give the standing wave representation of the incident field. Thus the scattered field of any object is given by

$$\begin{pmatrix} Scattered \\ Field \end{pmatrix} = (S - I) \begin{pmatrix} Incoming \\ Modes \end{pmatrix} \qquad \textbf{(64)}$$

For an antenna, the generalized scattering matrix is slightly more complicated than a typical target because all antennas have a port which connects the antenna to a receiver/transmitter which is represented by some load impedance Z_L. Therefore, for an antenna, the generalized scattering matrix relates incoming and outgoing spherical waves (b_i^+ and b_i^-) to each other and to the signals on the antenna transmission line (a^+ and a^-) which is illustrated in Figure 53. In Figure 53, S_{00} is the reflection coefficient at the transmission line-antenna interface looking from the termination toward the antenna. Similarly, Γ is the reflection coefficient at the transmission line-load interface looking from the antenna toward the load.
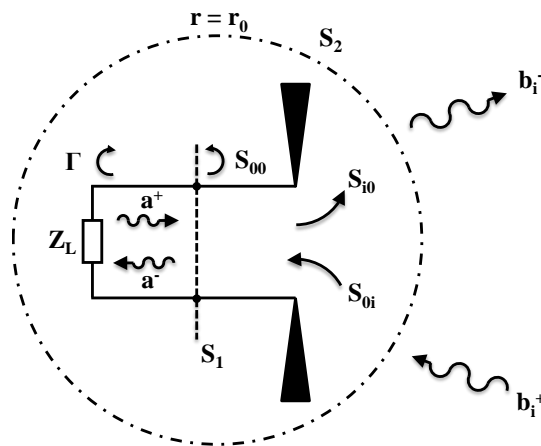
Figure 53 Illustration of the Generalized Scattering Matrix for an Antenna

Based on the illustration of Figure 53, the generalized scattering matrix has the form shown in Figure 54. From Figure 54 it is observed that the generalized scattering matrix consists of the antenna receive modal coefficients, the transmit coefficients, the reflection coefficient and the scattering matrix. Therefore, the generalized scattering matrix completely captures the radiation and scattering properties of an antenna which makes it a very useful tool for discussing antenna scattering for reasons that will become apparent in the following section.
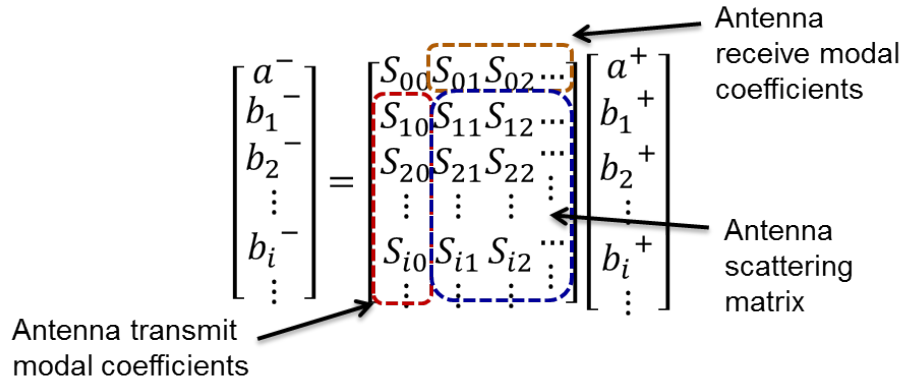
Figure 54 Generalized Scattering Matrix for an Antenna

5.2.2   Decomposition of Scattered Field

An antenna's scattering pattern is controlled by the amplitude and phase of the currents induced just like any other structure. However, antennas have two possible modes of scatter. Firstly, there is scattering caused by the shape, size and material (i.e. structural mode or residual mode) and this mode is independent of how the antenna receives or transmits energy (i.e. doesn't depend on transmit or receive modal coefficients). Secondly, there is scattering based on transmit/receive properties of antenna (i.e. antenna mode or load dependent mode) and this mode depends upon mismatch between antenna impedance and load impedance that is used to terminate antenna port. Therefore, the scattered field from an antenna can be decomposed into two basic terms which are most commonly referred to as the structural mode and the antenna mode. However, we will refer to these two terms as the residual mode/term and the load dependent mode/term because the commonly used terminology often leads to unnecessary confusion in the author's experience.

The decomposition of the scattered field can be written in terms of the modal components or the field components. For example, the scattered field in terms of modal components can be written as

$$b_S = b_S{}^0 - 0.5I(0)(1 - \Gamma_A)b_r \qquad (65)$$

In equation (65), $b_s{}^0$ is the residual mode and the remaining term is the load dependent term which depends upon the short circuit current $I(0)$, the reflection coefficient Γ_A and the receive modal coefficients b_r. Similarly, the scattered field can be expressed in terms of field components as follows

$$E_S(Z) = E_S(Z_L = 0) - 0.5I(0)(1 - \Gamma_A)E_r \qquad (66)$$

In equation x, the first term on the right hand side is the residual mode which only depends on E_s and corresponds to the scattered field when the antenna is short circuited. The second term on the RHS is the load dependent term which depends upon the radiated field E_r, the short circuit current and the reflection coefficient.

An important aspect concerning the decomposition of the scattered field is that it is not unique because it depends upon chosen reference impedance that is used to terminate the antenna port. There are three standard decompositions that are commonly found in the literature [19,20,21]. They are the short circuit (equation (67)), matched load (equation (68)) and complex conjugate match (equation (69)) decompositions and are given by the following equations.

The short circuit decomposition ($Z_L=0$) is given by

$$E_S(Z) = E_S(Z_L = 0) - 0.5I(0)(1 - \Gamma_A)E_r \qquad (67)$$

where the reflection coefficient is defined as

$$\Gamma_A \stackrel{\text{def}}{=} \frac{Z_A - Z_L}{Z_A + Z_L}$$

The matched load decomposition ($Z_L=Z_A$) is given by

$$E_S(Z) = E_S(Z_L = Z_A) + 0.5I(Z_A)\Gamma_A E_r \qquad (68)$$

where the reflection coefficient is the same as the short circuit decomposition.

The complex conjugate match ($Z_L=Z_A*$) decomposition is given by

$$E_S(Z) = E_S(Z_L = Z_A^*) + I(Z_A^*)\Gamma_A^* E_r \qquad (69)$$

where the reflection coefficient is define as

$$\Gamma_A^* \stackrel{\text{def}}{=} \frac{Z_A^* - Z}{Z_A + Z}$$

It is noted that throughout the remainder of this report that the complex conjugate matched decomposition (equation (69)) will be used because it is the most convenient decomposition to use when discussing antenna scattering and absorption.

5.2.3   Controlling Scattering

5.2.3.1   Two Basic Approaches for Controlling Scattering

One of the main advantages of decomposing the scattered field as discussed in section 5.2.2 is that it provides some physical insight into controlling scattering. All of the decompositions have two basic terms which are, there are two fundamental approaches for controlling scattering (i.e. achieving zero backscatter) [4,6]. They are the matched approach (MA) and the compensation/cancellation approach (CCA).

For the matched approach, scattering is minimized by minimizing the reflection coefficient over as large of bandwidth as possible which, in turn, minimizes the load dependent term. The residual term is then minimized by proper design of the antenna. Ideally, the reflection coefficient would be zero over the desired bandwidth but this physically impossible to achieve for passive lossless matching networks. Furthermore, this is not achievable with active matching

networks because of stability (i.e. attaching the same load to both ports of a non-Foster matching network results in an oscillator).

For the compensation/cancellation approach, scattering is minimized by using the load dependent term to cancel the residual term. This is accomplished with proper selection of the reflection coefficient which can easily be seen by rewriting equation (70) as follows

$$E_S(Z) = I(Z_A^*)E_r[E_S(Z_A^*)/I(Z_A^*)E_r - \Gamma_A^*] \qquad \textbf{(70)}$$

We can then define the first term inside the brackets of equation (70) as A which results in the following equation.

$$E_S(Z) = I(Z_A^*)E_r[A - \Gamma_A^*] \qquad \textbf{(71)}$$

From the above equation it is apparent that the scattered field can be minimized by minimizing the expression inside the brackets. However, the extent to which the scattered field can be controlled with this approach depends upon the magnitude of A. It can be shown [19] that if the magnitude of A is greater than one then no passive load can reduce total scattered field to zero, but a reactive load can be found to maximize or minimize the scattered field. If the magnitude of A is equal to one, then there is a passive reactive load that can reduce scattered field to zero [19]. When the magnitude of A is less than one, there is a dissipative load that can reduce scattered field to zero and a purely reactive load that will maximize scattering [19].

5.2.3.2 Achieving Zero Backscatter or Zero Total Scattered Power

Both approaches outlined in section 5.2.3.1 are equally valid for achieving zero backscatter or zero total power scattered. For the matched approach, this involves matching the antenna such that $\Gamma_A^* = 0$ and designing the antenna such that the residual mode has a null in the backscatter directions. For the compensation/cancellation approach, zero backscatter can be achieved by intentionally mismatching the antenna such that $\Gamma_A^* = A$. However, achieveing zero back scatter or zero total scattered power is inherently narrowband regardless of the approach used. For matched approach, a reflectionless matching network over any bandwidth is not physically realizable using passive and lossless devices [22] and such an active matching network would be unstable. For the compensation/cancellation approach, the reflection coefficient that provides minimum or zero scattering is a strong function of frequency and aspect angle. This can be seen from equation (70) where all components of A are frequency dependent and the field components are angle dependent. This makes it extremely difficult, if not impossible, to achieve zero backscatter over any finite bandwidth. However, at a single frequency it is possible to achieve zero backscatter using either approach. It is also possible to achieve zero total scattered power but this can only be accomplished at the expense of absorbed power which we will discuss in the following section.

5.2.3.3 Importance of Absorbed Power

Generally speaking, controlling scattering is only difficult if you are concerned about the absorbed power, in particular if you are trying to simultaneously maximize the absorbed power will minimizing the scattered power. The reason is that any antenna that absorbs power must also scatter power because the total power scattered is not independent of the absorbed power.

They are related to one another through the forward scattering theorem or optical theorem [23]. The forward scattering theorem (or optical theorem) is given by the following equation which states that the total extinction cross-section σ_{tot}, which is equal to the total scattering cross-section σ_s plus the absorption cross-section σ_a, is bounded by the forward scattering amplitude *f(0)*.

$$\sigma_{tot} = \sigma_s + \sigma_a = \frac{4\pi}{k} Im\{f(0)\} \tag{72}$$

From the equation above, it is apparent that the extinction cross-section cannot be zero unless both the forward scattering amplitude is zero. If the forward scattering amplitude is zero, this means that the scatter or antenna does not interact with the incident field. Therefore, it does not scatter the incident field but it also cannot absorb any power from the incident field because, if it did, the absorption cross-section would be greater than zero which leads to a contradiction.

There are two basic approaches for controlling scattering and absorption: 1) Minimize antenna scattering over all visible space (i.e. minimize total scattered power). 2) Minimize antenna scattering over a limited angular region of space. The first approach involves minimizing the extinction cross section which is subject to the fundamental bound given by the forward scattering theorem [23]. The second approach typically involves reducing the bistatic scattering from the antenna in the back half-space.

For the first approach, minimizing the total scattered power requires the antenna, or any object, to absorb more than it scatters [19,24]. To explain this fact it is beneficial to make use of the concept of absorption efficiency η which is define as follows

$$\eta = \frac{\sigma_a}{\sigma_a + \sigma_s} \tag{73}$$

where σ_s is the total scattering cross-section and σ_a the absorption cross-section which are defined as follows.

$$\sigma_a = 4\pi/D_a \tag{74}$$

$$\sigma_s = \frac{1}{4\pi} \iint \sigma_b d\Omega \tag{75}$$

In the above equations, D_a is the antenna directivity and σ_b is the bistatic scattering cross section. In minimizing the total scattered power we are effectively maximizing the absorption efficiency and, ideally, trying to make $\eta = 1$. In order for the absorption efficiency to approach one we need the scattered power to approach zero. However, we know from the forward scattering theorem that reducing the scattering cross-section also reduces the absorption cross-section because we are decoupling the antenna from the incident field. Therefore, it is possible for absorption efficiency to approach one if and only if the total scattering cross section approaches zero faster than the absorption cross section [19,24]. This results in a trade-off between the total scattered power and total absorbed power. That is, we can only reduce the total scattered power (or maximize absorption efficiency) if and only if we reduce the absorbed power. While this approach can be used to control scattering it leads to antennas that do not absorb as much power as they are capable of which, in most applications, is not desirable. However, one main benefit of this approach is that reducing total scattered power also reduces mutual coupling between

Approved for public release; distribution is unlimited.

antennas. Therefore, this approach can be used to reduce mutual coupling between antennas if desired.
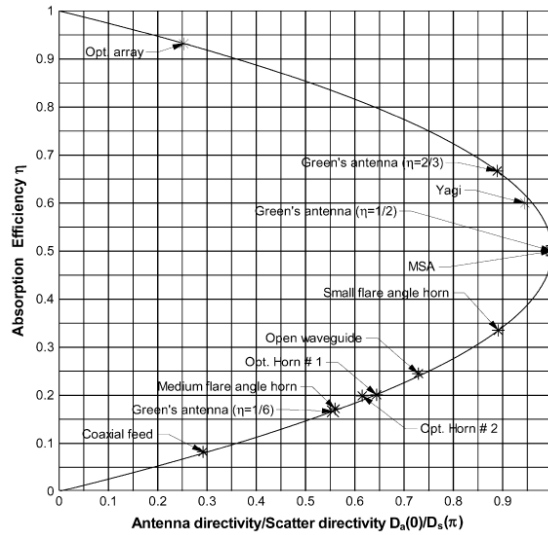
Figure 55 Absorption Efficiency as a Function of Antenna Directivity and Scatter Directivity from Reference [24]

For the second approach, we are interested in minimizing antenna scattering over only a limited angular region of space. This makes it possible to reduce scattering over a certain region without reducing the absorbed power. Ideally, the power scattered in the back half space would be zero while the absorbed power is maximized. For antennas that are capable of this behavior the total scattered power is greater than the absorbed power and, consequently, the antenna scatters strongly in the forward direction. In practice, scattering can be reduced over a limited solid angle with minimal to no reduction in absorbed power. This method relies on the fact that the antenna scattering pattern does not have to be the same as the transmit/receive pattern which is only true for multi-mode antennas. This concept is illustrated in Figure 56 which shows an antenna whose scattering pattern is the opposite of the transmit/receive pattern. As we will discuss in the following sections, a Huygens dipole source is capable of this behavior.
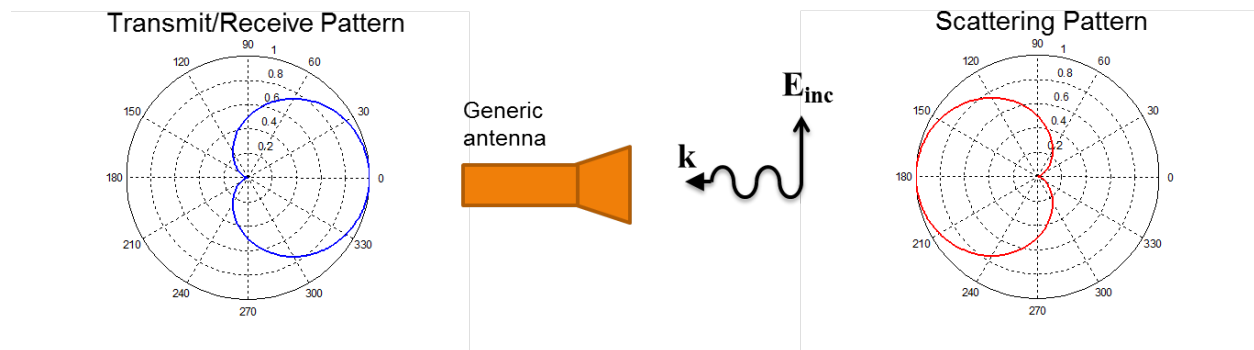
Figure 56 Illustration of Controlling Scattering Using Method 2

5.2.4 Generalized Scattering Matrix for an Ideal Huygens Dipole Source

In this section we will begin to discuss scattering from an ideal Huygens dipole source by first deriving the generalized scattering matrix for an ideal Huygens source. This will be followed by a discussion of the scattering properties and how effectively we can control the scattering from the Huygens source in in section 5.2.5.

A Huygens dipole source consists of orthogonal electric and magnetic dipole moments. This type of antenna is one of the simplest multi-mode antennas and it is possible to minimize scattering base on method 1 (total power scattered/absorption efficiency) or method 2 (limited solid angle). Also, the combination of electric and magnetic dipole moments naturally produces a null in its radiation and scattering pattern which can be utilized to achieve zero backscatter.

In general, only for simple cases (2 modes or less) can one obtain the generalized scattering matrix analytically. The conditions for which this is possible are there can only be two modes per port in the generalized scattering matrix and the symmetry and unitary properties must be applicable. Only under these conditions do we have enough degrees of freedom to determine the generalized scattering matrix analytically. In what follows, we are able to analytically derive the generalized scattering matrix for a Huygens source because we assume that the antenna is reciprocal and lossless. To derive the generalized scattering matrix for a Huygens source, let us first construct an ideal Huygens source from an x-directed electric dipole and a y-directed magnetic dipole as shown in Figure 57.
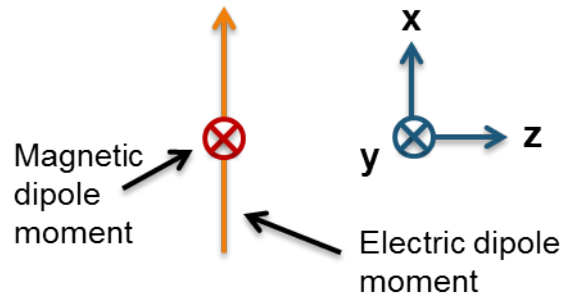
Figure 57 Illustration of the Geometry for a Crossed Electric and Magnetic Dipole Moment

We can construct the generalized scattering matrix by first considering the transmit case where each dipole mode is excited. We consider the most general case where the dipole modes have arbitrary excitation where the variable k is the ratio of the excitation or modal coefficients. Noting that there is a 90 degree phase difference between the radiated field from an electric and magnetic dipole, one way to write the partial scattering matrix is as follows

$$
\begin{pmatrix} 0 \\ 1 \\ \dfrac{1}{\sqrt{k^2+1}} \\ \dfrac{-jk}{\sqrt{k^2+1}} \end{pmatrix} = \begin{pmatrix} 0 & - & - \\ \dfrac{1}{\sqrt{k^2+1}} & - & - \\ \dfrac{-jk}{\sqrt{k^2+1}} & - & - \end{pmatrix} \begin{pmatrix} 1 \\ 0 \\ 0 \end{pmatrix}
\tag{76}
$$

where k is the ratio of the modal coefficients and is real ($0 \leq k \leq 1$) and the modal coefficients are normalized such that the total power radiated is always unity which is the origin of the

$1/\sqrt{k^2+1}$ term. On the left hand side (LHS) of equation (76), the top term is zero because under transmit conditions there is no reflected wave on the transmission line. The middle term in the column vector represents the magnetic dipole coefficient (m_{011}) and the third term the electric dipole coefficient (n_{011}). Using the symmetric and unitary properties, one finds that, for the matched case, the S-matrix must be

$$S = \begin{pmatrix} 0 & S_{12} & S_{13} \\ S_{12} & S_{13}S_{13}{}^{*}e^{j\alpha} & -S_{12}{}^{*}S_{13}e^{j\alpha} \\ S_{13} & -S_{12}{}^{*}S_{13}e^{j\alpha} & (S_{12}{}^{*})^2\dfrac{S_{13}}{S_{13}{}^{*}}e^{j\alpha} \end{pmatrix} \tag{77}$$

In this case the symmetry property ($S_{mn} = S_{nm}$ for m ≠ n) is a consequence of reciprocity and the unitary property ($[S][S]^{*} = [I]$) is a consequence of energy conservation for a loss-less passive system (we have assumed zero ohmic loss in this case). Substituting the S_{12} and S_{13} terms from equation (76) into equation (77) we obtain the generalized scattering matrix for an ideal Huygens source

$$S = \begin{pmatrix} 0 & \dfrac{1}{\sqrt{k^2+1}} & \dfrac{-jk}{\sqrt{k^2+1}} \\ \dfrac{1}{\sqrt{k^2+1}} & \dfrac{-jk^2}{k^2+1}e^{j\alpha} & \dfrac{k}{k^2+1}e^{j\alpha} \\ \dfrac{-jk}{\sqrt{k^2+1}} & \dfrac{k}{k^2+1}e^{j\alpha} & \dfrac{j}{k^2+1}e^{j\alpha} \end{pmatrix} \tag{78}$$

In equation (78), α is a phase angle that can be chosen arbitrarily.

5.2.5   Scattering from an Ideal Huygens Source

In this section we will obtain the scattered field from an ideal Huygens source and discuss the minimization of the total scattered power and the necessary conditions for zero backscatter. We begin by assuming an incident field of the form

$$\bar{E}_\iota = \hat{x}E_i e^{-j\beta z} \tag{79}$$

The scattered field is given by

$$E_S = (S - I)\begin{pmatrix} a^+ \\ b_1{}^+ \\ b_2{}^+ \end{pmatrix} \tag{80}$$

By substituting equation (77) into (80) and using the complex conjugate decomposition of the scattering field (equation (69)), the residual term can be written as

$$\bar{E}(Z_a{}^*) = \frac{\sqrt{3}}{4} \frac{E_i \lambda}{\sqrt{\eta \pi}} \begin{pmatrix} j - j\overline{S_{22}} + S_{23} \\ -1 - jS_{32} + S_{33} \end{pmatrix} \qquad (81)$$

and the load dependent term as

$$\Gamma I(Z_a{}^*)\overline{E_r} = \begin{pmatrix} 0 \\ \dfrac{\sqrt{3}}{4} \dfrac{E_i \lambda}{\sqrt{\eta \pi}} [-jS_{12} + S_{13}]\gamma S_{21} \\ \dfrac{\sqrt{3}}{4} \dfrac{E_i \lambda}{\sqrt{\eta \pi}} [-jS_{12} + S_{13}]\gamma S_{31} \end{pmatrix} \qquad (82)$$

Now that we have the scattered field from and ideal Huygens source we can demonstrate how scattering can be controlled using the methods outlined in section 5.2.3.3 for the cases where the antenna load is the complex conjugate of the antenna impedance and the case where it is not.

5.2.5.1 Total Scattered Power for the Complex Conjugate Matched Case

In this section we will discuss minimizing the total scattered power when the load impedance is the complex conjugate of the antenna impedance. We want to minimize total scattered power (max absorption efficiency) for a load impedance equal to the complex conjugate of the antenna impedance. Therefore, this is equivalent to simultaneously minimizing the total scattering power while maximizing the absorbed power or maximizing the absorption efficiency. For a complex conjugate match, the reflection coefficient is zero which reduces equation (69) to the following

$$\bar{E}(Z) = \bar{E}(Z_a{}^*) + \Gamma I(Z_a{}^*)\overline{E_r} \rightarrow \bar{E}(Z) = \bar{E}(Z_a{}^*) \qquad (83)$$

Therefore, the total scattered field is just the residual term from equation (69). We can use this to then compute total power scattered and the absorbed power as follows. The scattered power is given by

$$P_s = \sum_1^i |b_n{}^- - b_n{}^+|^2 \qquad (84)$$

Using equations (78) and (81), the total scattered power

$$P_s(Z_a{}^*) = \frac{3(E_i\lambda)^2}{16\eta\pi}\left\{ \left|j + \frac{k - k^2}{k^2 + 1}e^{j\alpha}\right|^2 + \left|-1 + j\frac{1 - k}{k^2 + 1}e^{j\alpha}\right|^2 \right\} \qquad (85)$$

The absorbed power is given by

$$P_a = |a^-|^2 = \left| \frac{\sqrt{3}}{4} \frac{E_i \lambda}{\sqrt{\eta \pi}} [-jS_{12} + S_{13}] \right|^2 \tag{86}$$

Using equation (78) in equation (85), the absorbed power is given by

$$P_a(Z_a^*) = \frac{3(E_i \lambda)^2}{16\eta \pi} \frac{(k+1)^2}{k^2 + 1} \tag{87}$$

To maximize the absorption efficiency we note that scattered power must be less than the absorbed power. In Figure 58 we have plotted the ratio of the total scattered power to the absorbed power as a function of the ratio of the modal coefficients k and the relative phase α. Because Ps must be less than Pa, the maximum of absorption efficiency must be located in the dark blue area in Figure 58. It turns out that the maximum absorption efficiency occurs for k ≈ 0.3 and α = 0.5π and it is approximately 67%. It is noted that the point where the absorption efficiency is maximized corresponds to a 22.5% reduction in absorbed power. That is, for a Huygens source, maximum absorbed power always occurs for k=1and it is independent of α which can easily be seen from equation (87). It is possible to increase the absorption efficiency if the antenna is not complex conjugate matched by proper choice of the load impedance. Of course, this will lead to a further reduction in absorbed power as discussed previously.
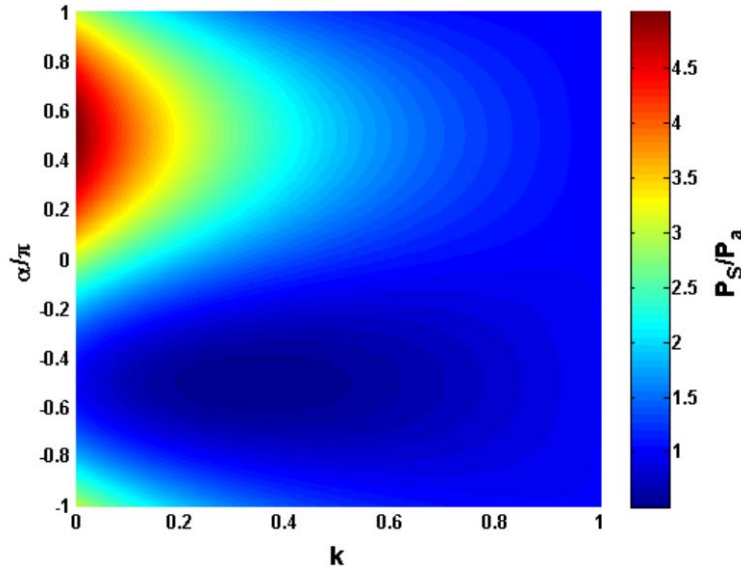
Figure 58 The Ratio of the Total Scattered Power to Total Absorbed Power as a Function of the Ratio of the Modal Coefficients k and the Relative Phase α

5.2.5.2   Zero Backscatter for the Complex Conjugate Matched Case

In this section we will discuss the condition for zero backscatter when the antenna is complex conjugate matched. We are interested in the zero backscatter condition for the complex

conjugate matched case because, under this matching condition, we have maximum absorbed power or power transfer to the load. Again, under this condition the reflection coefficient is zero which reduces scattering field from equation (69) to the following

$$\bar{E}(Z) = \bar{E}(Z_a{}^*) + \Gamma I(Z_a{}^*)\overline{E_r} \rightarrow \bar{E}(Z) = \bar{E}(Z_a{}^*) \tag{88}$$

The residual field term can be written using the modal functions as follows

$$\bar{E}(Z_a{}^*) = \frac{\sqrt{3}}{4}\frac{E_i\lambda}{\sqrt{\eta\pi}}(0 \quad m_{o11} \quad n_{e11})\begin{pmatrix} \overline{j} - jS_{22} + S_{23} \\ -1 - jS_{32} + S_{33} \end{pmatrix} \tag{89}$$

where m_{011} is the magnetic dipole field pattern and n_{011} is the electric dipole field pattern. Multiplying the column vector by the row vector in equation (89) and substituting the S-parameters of ideal Huygens source we have

$$\bar{E}(Z_a{}^*) = \frac{\sqrt{3}}{4}\frac{E_i\lambda}{\sqrt{\eta\pi}}\left[\left(j + \frac{k-k^2}{k^2+1}e^{j\alpha}\right)m_{o11} + \left(-1 + j\frac{1-k}{k^2+1}e^{j\alpha}\right)n_{e11}\right] \tag{90}$$

Under the far field condition (large argument approximation), the mode functions for the backscattered ($\theta = \pi$, $\phi = 0°$) field are

$$m_{o11} = \frac{-e^{-j\beta r}}{\beta r}\hat{\theta} \tag{91}$$

$$n_{e11} = -j\frac{e^{-j\beta r}}{\beta r}\hat{\theta} \tag{92}$$

Substituting equations (91) and (92) into equation (90), the backscattered field is given by

$$\bar{E}(Z_a{}^*) = \hat{\theta}\frac{\sqrt{3}}{4}\frac{E_i\lambda}{\sqrt{\eta\pi}}\frac{e^{-j\beta r}}{\beta r}\left[\frac{(k-1)^2}{k^2+1}e^{j\alpha}\right] \tag{93}$$

From equation (93) it is apparent that zero backscatter is only achievable for k=1 which corresponds to equal excitation of the electric and magnetic dipole modes. For this particular case, the backscattered field is not affected by the phasing between the electric and magnetic dipoles. This result is similar to the zero backscatter condition for small isotropic particles [25,26].

5.2.5.3 Zero Backscatter for an Arbitrary Load

In this section we will discuss the condition for zero backscatter when the antenna is matched to an arbitrary load impedance. For the case where the load impedance is not complex conjugate matched to the antenna impedance there is no value of k and/or α alone that can produce zero backscatter. For this case, zero backscatter can only be achieved by proper

mismatch which leads to a reduction in absorbed power. The reflection coefficient for which zero back scatter is obtained can be found using equations (81) and (82). First, equations (81) and (82) are multiplied by the electric and magnetic dipole modal functions (see equations (91) and (92)). Then we equate equations (81) and (82) and solve for the reflection coefficient γ which results in the following expression

$$\gamma = \frac{(k-1)^2}{(k+1)^2} e^{j(\alpha + 0.5\pi)} \tag{94}$$

From this expression it can be shown that the magnitude of γ is always less than or equal to one which means there is a passive reactive load or dissipative load that can reduce the backscattered field to zero. In this case, the backscattered field depends upon both k and α.

5.2.6 Realization and Implementation of a Zero Backscatter Huygens Source

In this section we discuss the realization and implementation of a zero backscatter Huygens source. To realize a Huygens source we must select of design an antenna that is capable of exciting and electric and magnetic dipole mode. There are a large number of electric and magnetic dipole antennas that can be found in the literature. However, there are far fewer combined electric and magnetic dipole antennas, particularly for scattering. Over the course of this project we have evaluated a large number of these for use in a low backscatter antenna. The most promising candidate is the folded multiarm spherical helix (FMSH) [27] which we will discuss in the following section. An example of the FMSH is shown in Figure 59 The Folded Multi-arm Spherical Helix (FMSH)

Figure 59 The Folded Multi-arm Spherical Helix (FMSH)

5.2.6.1 Folded Multiarm Spherical Helix (FMSH)

The folded multiarm spherical helix (FMSH) can support both the electric dipole and magnetic dipole mode [27,28] which makes it very attractive for use as a Huygens source. Additionally, it has been shown in [27] that the FMSH can approach the Chu-Wheeler-Thal radiation Q limit for an electric dipole.

The dominant mode of the FMSH can be either an electric dipole (TM) or magnetic dipole (TE) depending upon how the antenna is excited. If the top and bottom sections of an arm are driven 180deg out of phase the electric dipole mode is dominant because the far field contribution from the I_φ current components cancel. This excitation is illustrated in Figure 60. If the top and bottom sections are driven in phase (same potential) the magnetic dipole mode is dominant and the far field contribution from the I_θ current components cancel as illustrated in Figure 61.
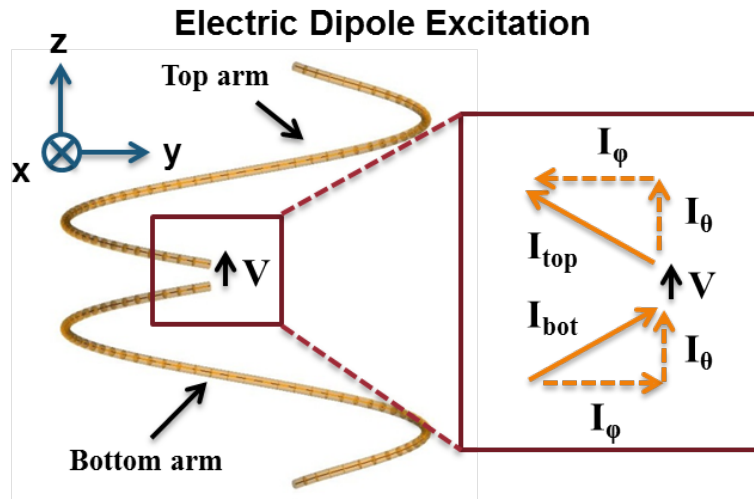
Figure 60 Electric Dipole Excitation of the Folded Multi-arm Spherical Helix (FMSH)
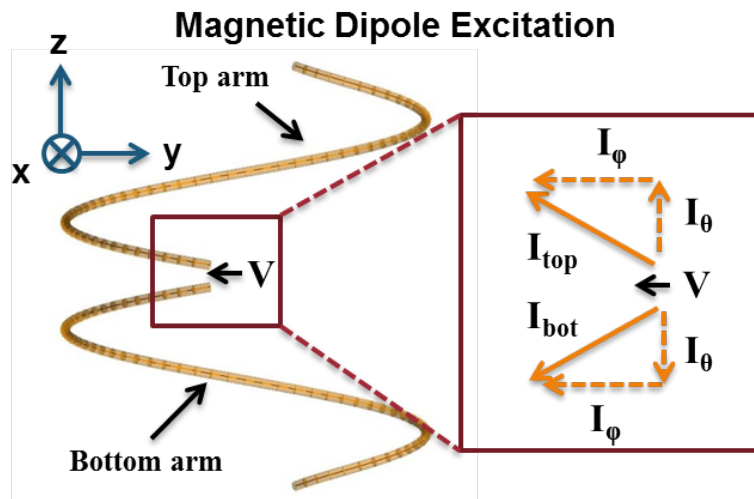
Figure 61 Magnetic Dipole Excitation of the Folded Multi-arm Spherical Helix (FMSH)

When it comes to realizing a Huygens source with the FMSH there are essentially two options. The first option is to use the same FMSH to excite both electric (TM) and magnetic (TE) dipole modes. As illustrated in Figure 62 this can be accomplished by using two feeds where both feeds are essentially dipoles. However, this configuration can't be used to achieve zero backscatter because the electric and magnetic dipole moments are parallel. In addition, this arrangement results in greater excitation of unwanted spherical modes than option 2

63
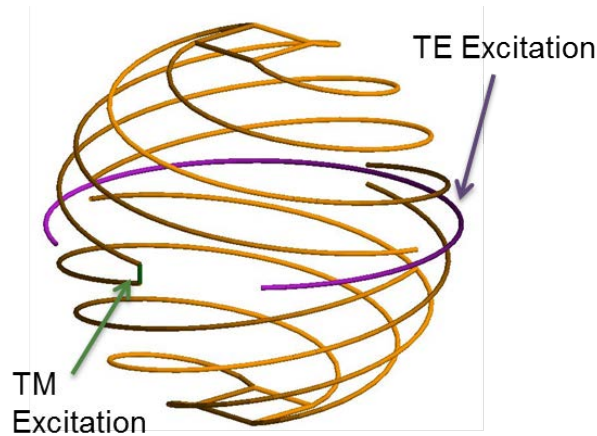
Figure 62 The Same FMSH Used to Excite Both Electric and Magnetic Dipole Modes

For the second option, the electric and magnetic dipole modes are excited by separate FMSHs with one being placed inside the other or nested. This leads to a configuration where the magnetic dipole FMSH (M-FMSH) can be inside electric dipole FMSH (E-FMSH) or vice versa (see Figure 63). It is known that a spherical electric dipole stores less energy inside (lower Q) than the corresponding spherical magnetic dipole. Therefore, one might assume the optimal arrangement might be the M-FMSH inside the E-FMSH. We will discuss this in more detail in section 5.2.6.3.
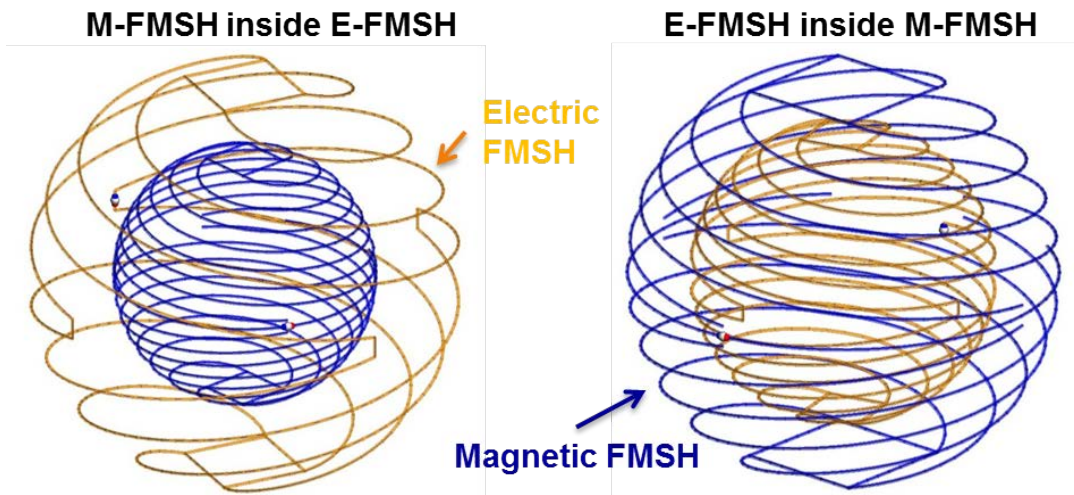
Figure 63 Two Nested FMSH Used to Eexcited Orthogonal Electric and Magnetic Dipole Moments

5.2.6.2 Implementation Issues

In realizing a Huygens source there are a number of issues that make implementation challenging regardless of the antenna type used to excite the magnetic and electric dipole modes. First of all, mode balance is extremely important for achieving zero backscatter. To achieve zero backscatter we require equal excitation of the electric and magnetic dipole modes which can be

Approved for public release; distribution is unlimited.

difficult because most antennas cannot strongly excite a magnetic dipole mode. That is, if you have two antennas are the same electrical size and one excites an electric dipole mode and the other a magnetic dipole mode, the electric dipole mode tends to be much stronger (i.e. a small wire dipole and small wire loop is classic example). Fortunately, the FMSH can be tuned to excite a magnetic dipole mode with similar strength as an electric dipole mode.

Another key issue is the excitation of unwanted higher order modes. While in theory it may be possible to achieve zero backscatter when higher order modes are present, from a practical point of view, it becomes significantly more difficult. Therefore, it is important to suppress the excitation of higher order modes. This is not typically a problem for electric dipole antennas but it is for magnetic dipole antennas because we must use electric charge to create a magnetic dipole moment. This would not be a problem if magnetic charge existed but, unfortunately it doesn't. A classic example of this is a small loop of electric current which excites a magnetic dipole moment. However, the excitation is not pure in that there is always an electric dipole moment whose strength depends on the electrical size of the loop.

Another important issue is coupling between the dipoles. Ideally, there is no coupling between an electric and magnetic dipole when they are co-located. However, the presence of higher order modes can lead to coupling. Also, the feeds used to excite the dipoles can produce coupling and there can also be coupling between the feed networks of each dipole. All of these make achieving the proper mode balance more difficult. In the case of feed network coupling, it can also lead to additional terms in the scattered field that must be compensated in some manner.

The last main issue is the relative phasing between electric and magnetic dipole modes. In order to achieve zero backscatter we must maintain a 90 degree phase shift between the dipoles. Any deviation from this will increase the backscatter.

5.2.6.3 Huygens Source Realization using FMSH

In this section we will show how the implementation issues discusses in section 5.2.6.2 can be addressed using the FMSH antenna to realize a Huygens source. Firstly, achieving the desired mode balance is essentially reliant on controlling the resonant frequency of both dipoles and matching. For the FMSH, there are a number of variables for controlling the resonant frequency which are electrical size (with respect to the free space wavelength), number of arms, number of turns, termination/connection of arms, feed dipole length (M-FMSH only). Therefore, achieving the proper mode balance is achievable (see Figure 65 and Figure 67). To demonstrate this, let us first consider the case were the M-FMSH is inside the E-FMSH as shown in Figure 64. For this case, both dipole modes have been tuned to resonate around an electrical size of ka ~ 0.395. Figure 65 shows how the power radiated is distributed amongst the mode modes excited by the Huygens source. These results were obtained numerically using the integral equation based software FEKO [29]. From Figure 65 it is evident that most of the power is in the electric and magnetic dipole mode which means that higher order modes are negligible over the frequency range shown in the figure. Furthermore, it is evident that there is equal excitation (equal power) of both modes near the resonant frequency. Outside resonant region, there is a large modal power imbalance between electric and magnetic dipole modes and the antenna almost behaves as a single mode antenna. This behavior is not desirable because we need equal excitation of the modes to achieve zero backscatter. Therefore, the Huygens source in Figure 64 is fairly narrowband.
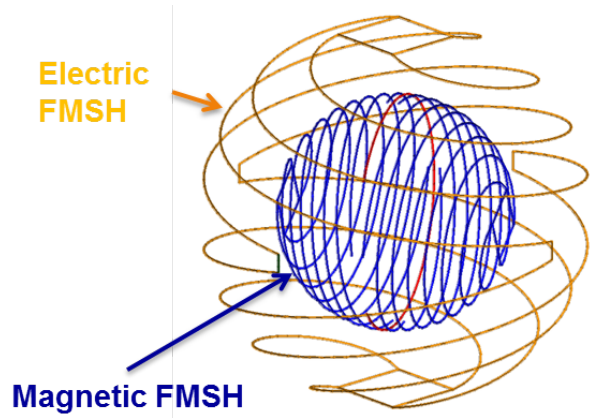
Figure 64 Magnetic Dipole FMSH Inside an Electric Dipole FMSH
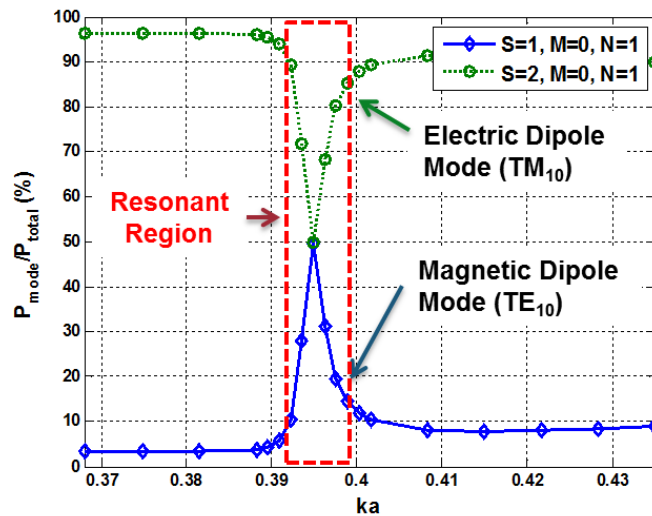
Figure 65 Modal Power for Magnetic Dipole FMSH Inside an Electric Dipole FMSH

Let us next consider the opposite case where the E-FMSH is inside the M-FMSH as shown in Figure 66. Again, in the resonance region we have equal excitation of the electric and dipole modes as shown in Figure 67. Outside the resonant region there is a small modal power imbalance between electric and magnetic dipole modes. Therefore, this implementation of the Huygens source is potentially more broadband than the former. However, for this implementation, higher order modes outside resonant region are not as negligible as the former antenna. The main issue is the dipole feed for the M-FMSH.
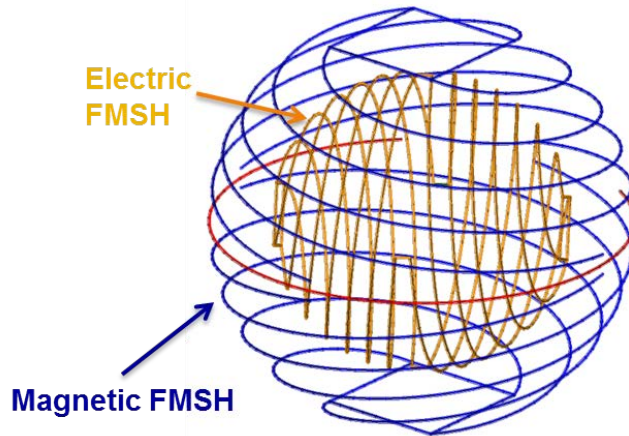
Figure 66 Electric Dipole FMSH Inside a Magnetic Dipole FMSH
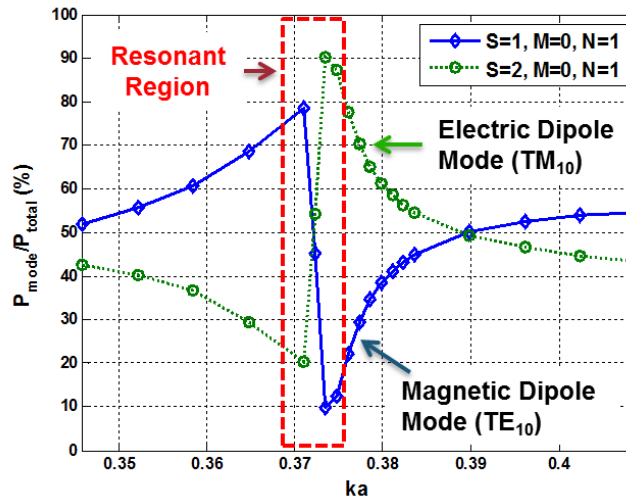
Figure 67 Modal Power for Electric Dipole FMSH Inside a Magnetic Dipole FMSH

When it comes to mitigating the excitation of higher order modes in the FMSH, the electric dipole version functions extremely well as shown in Figure 68. The results shown in Figure 68 are based on a single excitation of a single pair of arms. However, each pair of arms can be excited to further suppress higher order modes as the electrical size increases. The magnetic dipole version of the FMSH functions well as a magnetic dipole but the dipole feed excites additional modes outside the resonant region as shown in Figure 69. This is an inherent problem with the magnetic dipole version of the FMSH but, to some degree, this can be addressed by adjusting length of feed dipole but this also affects the resonant frequency.

67
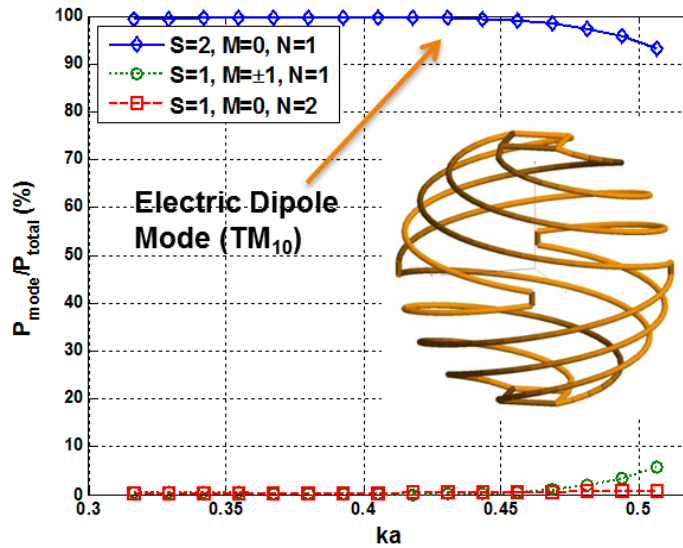
Figure 68 Modal Power for FMSH with Electric Dipole Moment Excited
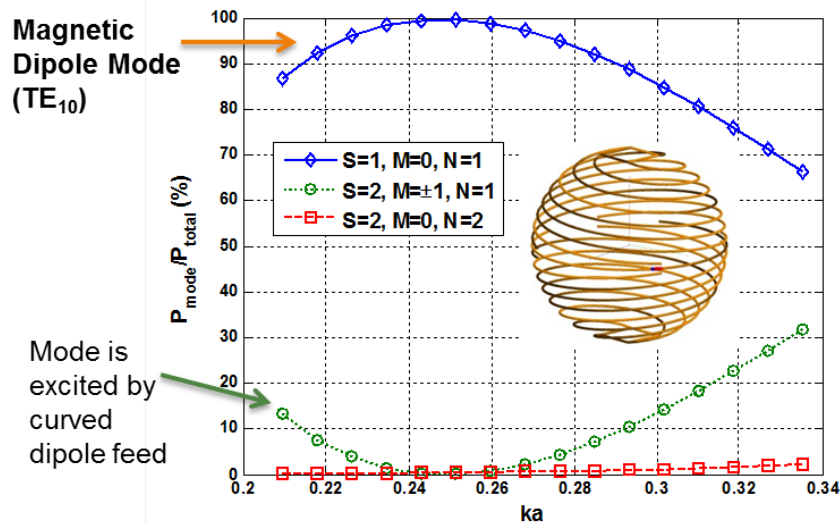
Figure 69 Modal Power for FMSH with Magnetic Dipole Moment Excited

We know demonstrate that it is possible to use the FMSH to realize a Huygens source with zero backscatter. In Figure 70 the total scattered field in the yz and xy planes is plotted for the Huygens source in Figure 66 at the resonant frequency. As you can see from Figure 70, in the backscatter direction (θ=90 degrees) the scattered field has been greatly reduced but it is not zero. In practice, we will never achieve zero backscatter numerically and it is a very tedious process that involves a lot of fine tuning to reduce the backscatter to a very low level but it is possible.
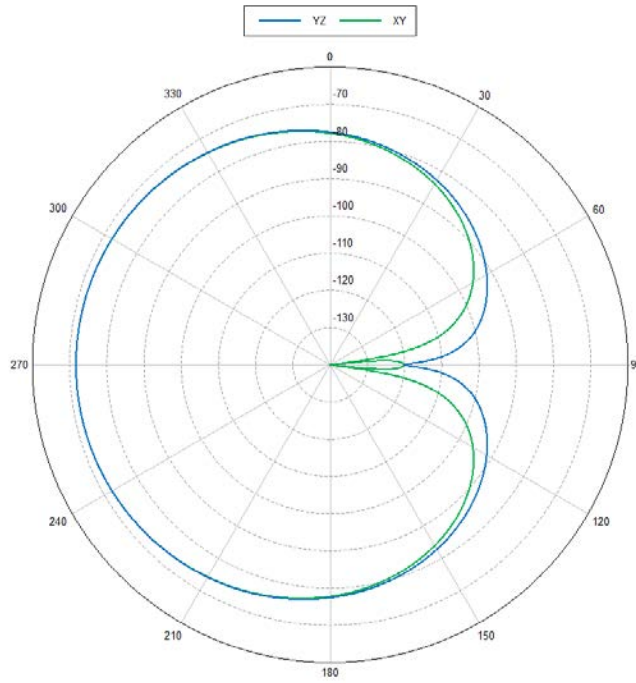
Figure 70 Scattering Patterns in the YZ-Plane and XZ-Plane for a Huygens Source

Approved for public release; distribution is unlimited.

6 REFERENCES

[1] R. T. Compton Jr., *Adaptive Antennas: Concepts and Performance*.: Prentice Hall, 1988.

[2] COMSOL. [Online]. http://www.comsol.com

[3] ANSYS HFSS. [Online]. http://www.ansys.com

[4] J. J. Zhang, Y. Luo, H. S. Chen, and B.-I. Wu, "Manipulating the directivity of antennas with metamaterial," *Optics Express*, vol. 16, pp. 10962-10967, 2008.

[5] J. B. Pendry, D. Schurig, and D. R. Smith, "Controlling electromagnetic fields," *Science*, vol. 312, pp. 1780-1782, 2006.

[6] U. Leonhardt and T. G. Philbin, "General relativity in electrical engineering," *New J. Phys.*, vol. 8, p. 247, 2006.

[7] L. J. Chu, "Physical limitations of omni-directional antennas," *J. Appl. Phys.*, vol. 19, pp. 1163-1175, 1948.

[8] B. L. Zhang, B.-I. Wu, and H. S. Chen, "High directive antenna with virtual aperture," in *Proc. IEEE APS International Symposium*, Charleston, 2009.

[9] J. A. Kong, *Electromagnetic Wave Theory*. Cambridge: EMW, 2008.

[10] A. V. Kildishev, W. Cai, U. K. Chettiar, and V. M. Shalaev, "Transformation optics: approaching broadband electromagnetic cloaking," *New J. Phys.*, vol. 10, p. 115209, 2008.

[11] W. C. Chew, *Waves and Fields in Inhomogeneous Media*. Piscataway: IEEE Press, 1995.

[12] H. S. Chen, B.-I. Wu, B. L. Zhang, and J. A. Kong, "Electromagnetic wave interactions with a metamaterial cloak," *Phys. Rev. Lett.*, vol. 99, p. 063903, 2007.

[13] B. L. Zhang, H. S. Chen, B. I. Wu, and J. A. Kong, "Extraordinary surface voltage effect in the invisibility cloak with an active device inside," *Phys. Rev. Lett.*, vol. 100, p. 063904, 2008.

[14] M. Abramowitz and I. Stegun, *Handbook of Mathematical Functions*. New York: Dover, 1965.

[15] B. L. Zhang, *Electromagnetics of Transformation Media*. Cambridge: MIT, 2009.

[16] Y. Ra'di, V. S. Asadchy, and S. A. Tretyakov, "Total Absorption of Electromagnetic Waves in Ultimately Thin Layers," *IEEE Transactions on Antennas and Propagation*, vol. 61, no. 9, pp. 4606-4616, September 2013.

[17] J. Vehmas, Y. Ra'di, A. O. Karilainen, and S. A. Tretyakov, "Eliminating Electromagnetic Scattering From Small Particles," *IEEE Transactions on Antennas and Propagation*, vol. 61, no. 7, pp. 3747-3756, July 2013.

[18] I. Liberal, I. Ederra, R. Gonzalo, and R. W. Ziolkowski, "A Multipolar Analysis of Near-Field Absorption and Scattering Processes," *IEEE Transactions on Antennas and Propagation*, vol. 61, no. 10, pp. 5184-5199, October 2013.

[19] R.B. Green, The General Theory of Antenna Scattering, 1963, Ph.D. Dissertation, The Ohio State University, Columbus OH.

[20] R.C. Hansen, "Relationships Between Antennas as Scatterers and as Radiators," *Proc. IEEE*, vol. 77, pp. 659-662, May 1989.

[21] M. T. Tuley, "Antenna RCS and RCSR," in *Radar Cross Section*.: SciTech Publishing,

2004, ch. 10, pp. 407-447.

[22] R. M. Fano, Theoretical Limitations on the Broadband Matching of Arbitrary Impedances, 1941, PhD thesis, MIT.

[23] M. Born and E. Wolfe, *Principles of Optics*, 7th ed.: Cambridge University Press, 1999.

[24] J. B. Andersen and A. Frandsen, "Absorption Efficiency of Receiving Antennas," *IEEE Transactions on Antennas and Propagation*, vol. 53, no. 9, pp. 2843-2849, September 2005.

[25] V.H. Weston, "Theory of absorbers in scattering," *IEEE Transactions on Antennas and Propagation*, vol. 11, no. 5, pp. 578-584, September 1963.

[26] R. J. Wagner and P. J. Lynch, "Theorem on Electromagnetic Backscatter," *Phys. Rev.*, vol. 131, pp. 21-23, 1963.

[27] S.R. Best, "The Radiation Properties of Electrically Small Folded Spherical Helix Antennas," *IEEE Transactions on Antennas and Propagation*, vol. 52, no. 4, April 2004.

[28] O. S. Kim, "Low-Q Electrically Small Spherical Magnetic Dipole Antennas," *IEEE Transactions on Antennas and Propagation*, vol. 58, no. 7, July 2010.

[29] FEKO - EM Simulation Software. [Online]. http://www.feko.info

[30] Junho Yeo, Ji-Fu Ma, and Raj Mittra, "GA-Based Design of Artificial Magnetic Ground Planes (AMGs) Utilizing Frequency-Selective Surfaces For Bandwidth Enhancement Of Microstrip Antennas," *Microwave and Optical Tech. Letters*, vol. 44, no. 1, pp. 6-13, January 2005.

[31] S. R. Best and D. L. Hanna, "Design of a Broadband Dipole in close Proximity to an EBG Ground Plane," *IEEE Ant. and Prop. Magazine*, vol. 50, no. 6, December 2008.

[32] J. A. Stratton, *Electromagnetic Theory*. Piscataway: IEEE Press, 2007.

[33] B.-I. Wu, T. M. Grzegorczyk, Y. Zhang, and J. A. Kong, "Guided modes with imaginary transverse wavenumber in a slab waveguide with negative permittivity and permeability," *J. Appl. Phys.*, vol. 93, pp. 9386-9389, 2003.

[34] J. Lu et al., "Effect of poles on subwavelength focusing by an LHM slab," *Microwave Opt. Technol. Lett.*, vol. 45, pp. 49-53, 2005.

List of Acronyms, Abbreviations, and Symbols

Acronym	Description
AFRL	Air Force Research Laboratory
AMG	Artificial Magnetic Grounds
CM	Characteristic Modes
CSWAP	Cost, Size, Weight and Power
D	Directivity
dB	Decibels
EBG	Electronic Bandgap
EM	Electromagnetic
FEM	Finite Element Method
FMSH	Folded Multi-arm Spherical Helix
FY	Fiscal Year
GHz	Gigahertz
GRIN	Graded Index
HFSS	High Frequency Structural Simulator
MHz	Megahertz
NEMO	Numerical Electromagnetic Optimizer
Ω	Ohms
PEC	Perfect Electric Conductor
PMC	Perfect Magnetic Conductor
PO	Physical Optics
Q	Quality Factor
STO	Source Transformation Optics
TE	Transverse Electric
TM	Transverse Magnetic
TO	Transformation Optics
UAS	Unmanned Aircraft System
λ	Wavelength